J. Fluid Mech. (2017), *vol.* 829, *pp.* 621–658. © Cambridge University Press 2017
doi:10.1017/jfm.2017.510

Two tandem cylinders of different diameters in cross-flow: flow-induced vibration

Bin Qin[1,2], Md. Mahbub Alam[1,2,†] and Yu Zhou[1,2]

[1]Institute for Turbulence–Noise–Vibration Interaction and Control, Shenzhen Graduate School, Harbin Institute of Technology, Shenzhen, China

[2]Digital Engineering Laboratory of Offshore Equipment, Shenzhen, China

(Received 29 December 2016; revised 14 June 2017; accepted 23 July 2017; first published online 22 September 2017)

This paper presents a systematic study of the cross-flow-induced vibration on a spring-supported circular cylinder of diameter D placed in the wake of a fixed cylinder of smaller diameter d. The ratios d/D and L/d are varied from 0.2 to 1.0 and from 1.0 to 5.5, respectively, where L is the distance between the centre of the upstream cylinder to the forward stagnation point of the downstream cylinder. Extensive measurements are conducted to capture the cylinder vibration and frequency responses, surface pressure, shedding frequencies and flow fields using laser vibrometer, hot-wire, pressure scanner and particle image velocimetry techniques. Six distinct flow regimes are identified. It has been found that a violent vibration may erupt for the spring-supported cylinder, and its dependence on d/D and L/d is documented. A careful examination and analysis of the flow structure, along with the simultaneously captured pressure distribution around and vibration of the downstream cylinder, cast light upon the mechanisms behind this vibration and its sustainability. The roles of added mass, flow-induced damping and physical aspects in the process of initiating the vibration are discussed in detail.

Key words: flow–structure interactions, vortex interactions, wakes

1. Introduction

Flow-induced vibration (FIV) of cylindrical structures is of both fundamental and practical significance. Industrial and engineering architectures are often the combinations of multiple cylindrical structures, such as cables of cable-stayed bridges, groups of chimney stacks, tubes in heat exchangers, transmission line bundles, masts, chemical reaction towers, offshore platforms, risers, undersea pipelines, adjacent skyscrapers, etc. Naturally, it is of practical importance to understand the proximity effect on FIV associated with a group of cylindrical structures. There have been a rather large number of investigations on flow around two cylindrical structures, which is the simplest configuration of multiple structures. Please refer to Zhou & Alam (2016) for a recent compendium on this topic. Two cylinders can be arranged in tandem, side-by-side or staggered. The interaction between two tandem cylinders is very strong (Hori 1959), involving shear layer reattachment, shear layer interference,

† Email addresses for correspondence: alam@hit.edu.cn, alamm28@yahoo.com

quasi-periodic vortices, vortex impingement, recirculation, etc. As such, this flow provides an excellent model for understanding the flow physics of further structures. While some structures are fixed, supported and rigid enough, not prone to FIV, others are elastic or flexibly supported and are subjected to FIV.

Most of the previous investigations have been performed on two fixed rigid circular cylinders of identical diameter ($d/D = 1$), focusing on the flow structure (Lin, Yang & Rockwell 2002; Jester & Kallinderis 2003; Zhou & Yiu 2006; Carmo, Meneghini & Sherwin 2010), fluid forces (Arie *et al.* 1983; Ljungkrona, Norberg & Sunden 1991; Alam *et al.* 2003; Alam 2016), Strouhal numbers (Igarashi 1981, 1984; Xu & Zhou 2004; Alam & Meyer 2013), etc. The wake of two tandem cylinders is in general classified into three regimes, depending on L/d (Zdravkovich 1987), where L is the distance from the upstream cylinder centre to the forward stagnation point of the downstream cylinder. (i) The overshoot flow regime occurs at $L/d = 0.5$–1.0, characterized by the overshoot of the free shear layers, separated from the upstream cylinder, over the downstream cylinder. (ii) The reattachment flow regime takes place at $L/d = 1.0$–3.5, where the separated free shear layers reattach on the downstream cylinder. (iii) The co-shedding flow regime refers to the case of $L/d > 3.5$, where the separated shear layers roll up alternately, forming vortex streets in the gap between, as well as behind, the cylinders. Alam *et al.* (2003) further divided the reattachment regime into alternate reattachment ($1.0 < L/d \leqslant 2.5$) and steady reattachment ($2.5 < L/d \leqslant 3.5$). The reattachment may occur on the downstream or upstream side of the downstream cylinder, depending on L/d (Zhou & Yiu 2006) and Reynolds number Re (Xu & Zhou 2004; Zhou *et al.* 2009), where Re is based on D and free-stream velocity U_∞. Alam & Zhou (2008) examined the vortex shedding frequency behind two tandem cylinders of different diameter ($d/D = 0.24$–1.0) at a given L/d ($= 5.5$). Two distinct vortex frequencies were detected behind the downstream cylinder. One was the same as detected in the gap between the cylinders, and the other was of relatively low frequency, ascribed to vortex shedding from the downstream cylinder.

Bokaian & Geoola (1984*a*) investigated the FIV of a cylinder placed in the wake of an identical upstream cylinder, where the downstream cylinder is spring-mounted and free to vibrate transversely. The mass damping ratio $m^*\zeta$ of the system was 0.109, where m^* is the ratio of the cylinder mass to the cylinder-displaced fluid mass, and ζ is the damping ratio. Depending on L/d, four different dynamic responses were found: galloping only ($L/d = 0.59$), vortex excitation (VE) only ($L/d > 2.5$), separated vortex excitation and galloping ($1.5 < L/d < 2.5$), and combined VE and galloping ($L/d = 1.0$). The VE corresponds to the occurrence of vibration near the reduced velocity $U_r (= U_\infty/f_n D)$ at which the natural vortex shedding frequency f_v coincides with the natural frequency f_n of the fluid–cylinder system. At VE, f_n and f_v are locked in with each other. The galloping persists for higher U_r corresponding to a much higher f_v than f_n, which is also called wake-galloping (Cooper & Wardlaw 1971). Brika & Laneville (1997, 1999) and Laneville & Brika (1999) examined the response of a downstream cylinder to a stationary or vibrating upstream cylinder for $L/d = 6.5$–24.5, $U_r = 4$–25 and $m^*\zeta = 0.00007$. For the stationary upstream cylinder, the response of the downstream cylinder was strongly dependent on L/d; the VE regime became wider and shifted to lower U_r. The cylinder exhibited a combination of VE and galloping for $L/d = 6.5$–8.0. Hover & Triantafyllou (2001) at $m^*\zeta = 0.12$ performed an investigation on the forces on a spring-mounted downstream cylinder for $L/d = 4.25$. Both VE and galloping were observed as U_r was varied from 2 to 17 by changing f_n via varying the cylinder

mass and/or spring stiffness at a given Re ($= 3.05 \times 10^4$). They noted an increase in the time-averaged drag coefficient C_D and fluctuating drag coefficient C_{Df} by approximately two times in the VE and galloping regimes. While growing in the VE regime, the fluctuating lift coefficient C_{Lf} dropped with increasing U_r during galloping. Kim *et al.* (2009) investigated the flow-induced vibration characteristics of two tandem circular cylinders for $L/d = 0.6$–3.7, $U_r = 1.5$–26 and $m^*\zeta = 0.65$. The response characteristics of the cylinders were classified into five regimes based on L/d: in regimes I ($0.6 \leqslant L/d < 0.7$) and IV ($2.5 \leqslant L/d < 3.2$), the cylinder vibration was insignificant; in regime II ($0.7 \leqslant L/d < 1.1$), both cylinders vibrated appreciably for $U_r > 6$, and the upstream one experienced a divergent vibration; and both cylinders showed convergent vibrations at $U_r \approx 6.7$ and vibrated like an isolated cylinder at $U_r \approx 6$ in regimes III ($1.1 \leqslant L/d < 2.5$) and V ($L/d \geqslant 3.2$), respectively. Mahir & Rockwell (1996) studied the flow structure around two cylinders that were forced to vibrate in in-phase or out-of-phase mode. Assi, Bearman & Meneghini (2010) investigated the vibration of a downstream cylinder ($m^*\zeta = 0.018$) for $L/d = 3.5$–5.5 where the vortices were generated in the gap between the cylinders. They observed the divergent galloping vibration when the vibration grows with increasing U_r. Assi *et al.* (2013) introduced wake stiffness, a consequence of the fluid forces. The wake stiffness concept suggested a decreasing vibration frequency with L/d, which increased in reality. They experimentally observed galloping vibration but failed to unearth the initiation of the vibration. All investigations discussed above involve two identical cylinders. In fact, previous studies on the FIV of two tandem cylinders have mostly been conducted for two cylinders of identical diameter at a low $m^*\zeta$ value.

There are only a few studies where the FIV on cylinders of different diameters ($d/D \neq 1.0$) has been investigated. Lam & To (2003) performed an experimental study where the downstream cylinder was flexible and smaller in diameter than the upstream cylinder (i.e. $d/D = 2.0$). No vibration was observed, although the value of $m^*\zeta$ was small, 0.002. The observation was attributed to the fact that the upstream cylinder of larger diameter acted to shelter the downstream cylinder. Rahmanian *et al.* (2012) performed a numerical simulation on the vortex-induced vibrations of two cylinders of $d/D = 0.1$ where the cylinders were mechanically coupled, behaving as one combined cylinder. The interaction between the coupled cylinders led to a very irregular vibration of the bundle in both the streamwise and cross-flow directions. Huang & Sworn (2013) at $m^*\zeta = 0.02$ investigated the fluid–structure interaction between pairs of flexible cylinders of $d/D = 4.0$, 2.0 and 1.0, that is, the upstream cylinder was again larger. The measurement results were very limited.

In spite of these investigations, a systematic study has never been conducted on the flow-induced response of the downstream cylinder, especially for $d/D < 1.0$. As such, many issues remain to be addressed. For example, although the L/d ranges are documented for the VE or wake-galloping, it is not clear how the vibrations are initiated. Furthermore, the dependence of the cylinder vibration on L/d and d/D is not documented, especially when $d/D < 1$. Then, what roles do the added mass, added damping and energy transfer play in generating the vibration? Would the wake structure mutate when the cylinder vibration amplitude grows? All these issues warrant the present investigation.

This work aims to study experimentally the flow-induced vibration of a cylinder in the presence of an upstream fixed cylinder. The downstream cylinder is spring-supported and free to oscillate only transversely. The d and L are varied, with an unchanged D, so that d/D and L/d may take values from 0.2 to 1.0 and from 1.0 to 5.5, respectively. The vibration response of the cylinder is systematically measured

for $U_r = 3.8$–44. One focus is on how cylinder vibration is initiated. The vortex shedding frequencies behind and in the gap between the cylinders are examined. Furthermore, the gap and wake flows are captured using time-resolved particle image velocimetry (PIV) for selected L/d and d/D for different reduced velocities in order to understand the mechanisms behind violent structural vibration. Finally, the cylinder displacement and lift force are simultaneously measured and analysed to gain insight into the underlying vibration mechanisms and flow physics.

2. Experimental details

Experiments were performed in a low-speed, closed-circuit wind tunnel with a test section of 5.6 m in length, 0.8 m in width and 1.0 m in height. Two cylinders were mounted in tandem in the horizontal mid-plane of the test section. Figure 1 shows a schematic of the experimental set-up, definitions of symbols and coordinates (x', y', z') and (x, y, z), with the origins defined at the upstream- and downstream-cylinder centres at the mid-span, respectively, both following the right-hand system. The downstream cylinder was hollow, made of Plexiglas, with the outer diameter $D = 40$ mm, inner diameter 36 mm and length $l = 740$ mm. Then $m^* = m/m_f = 4m/(\pi\rho D^2 l)$ was 275, where m is the total vibrating mass, m_f is the mass of fluid displaced by the cylinder and ρ is the density of the fluid. The diameter d was 8, 16, 24, 32 and 40 mm, corresponding to $d/D = 0.2$, 0.4, 0.6, 0.8 and 1.0, respectively. The first two of the upstream cylinders were made of steel, and the others were made of Plexiglas. The upstream cylinder was fixed at both ends on the wind-tunnel sidewalls. By shifting the upstream cylinder position, L/d took the values 1.0, 1.5, 2.0, 2.5, 3.0, 3.5, 4.0 and 5.5. The blockage is approximately 3.7 % and the aspect ratio of the monitoring (downstream) cylinder is $l/D = 18.5$. The downstream cylinder and spring system were supported at each end by two spiral springs made of steel, as shown in figure 1(*c*). The downstream cylinder and spring system was also supported at each end via an aluminium shaft of 6 mm diameter on one cantilever-mounted 1 mm thick leaf spring made of brass (figure 1*a*,*b*). As such, the cylinder could vibrate only transversely. To avoid interference and/or complexities caused by the end of the cylinder, end plates were fitted on both sides. Each end plate consisted of a rectangular slot of 12 mm × 80 mm at the downstream cylinder position to ensure enough clearance for the cylinder vibration. The cylinder displacement Y was measured using a laser vibrometer (OFV-505/5000, Polytec), which may resolve a displacement of 0.05 μm. The cylinder vibration frequency was obtained from a fast Fourier transform (FFT) based on the power spectral density function E_Y of Y. The free-stream velocity U_∞ was varied from 1.8 to 20.6 m s^{-1}, corresponding to $U_r = 3.8$–44 and $Re = 4.8 \times 10^3$ to 5.5×10^4. The turbulent intensity for this range of velocity was less than 0.3 %.

The characteristic properties, i.e. $\zeta = (\delta/2\pi)/\sqrt{1 + (\delta/2\pi)^2}$ and f_n, of the model were estimated from the cylinder displacement signal and power spectrum (figure 2) measured using the laser vibrometer when the cylinder was plucked in still air, where δ (= 0.0132) is the logarithmic decrement of displacement. The values of ζ and f_n were 0.0021 and 11.72 Hz (figure 2*b*), respectively, yielding $m^*\zeta = 0.58$.

Two hot wires were used to measure the streamwise fluctuating velocities u_1 and u_2, one (HT1) placed in the gap at $(x'/d, y'/d, z'/d) = (1, 1, 0)$ and the other (HT2) behind the downstream cylinder placed at $(x/D, y/D, z/D) = (4, -1, 0)$. HT2 was traversed along the streamwise direction to examine the flow evolution. The hot-wire signals are offset, low-pass-filtered, amplified and then digitized using a 16-channel analogue/digital board at the sampling frequency of 3 kHz. The sampling duration is

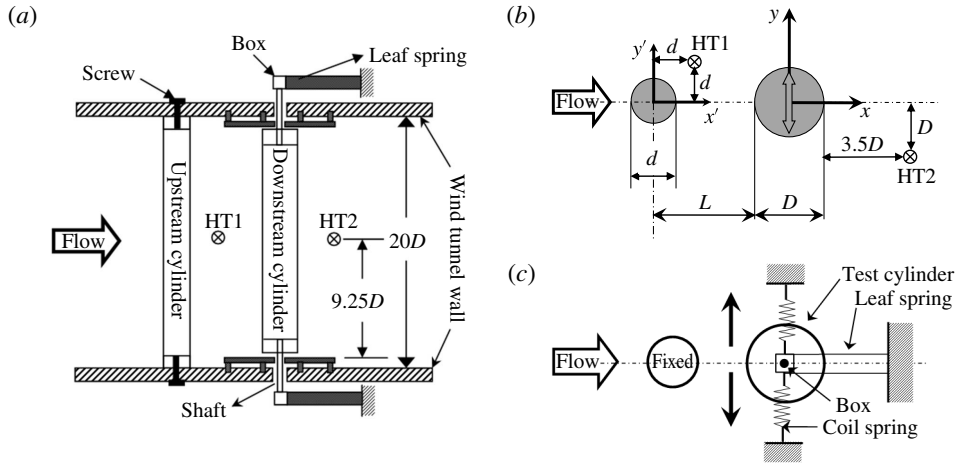

FIGURE 1. (*a*) Experimental set-up, (*b*) definitions of symbols and (*c*) the test cylinder support system.

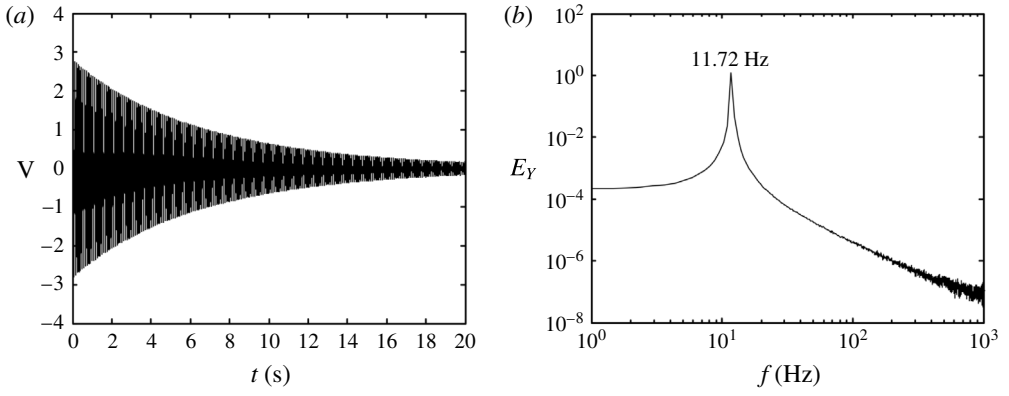

FIGURE 2. (*a*) Signal from a laser vibrometer after a plucking excitation, and (*b*) power spectrum of the displacement signal.

20 s for each record. The power spectral density functions E_{u1} and E_{u2} of u_1 and u_2 are calculated using the FFT algorithm. The frequency resolution in the power spectra is approximately 0.7 Hz.

A Dantec high-speed two-dimensional PIV system (Litron LDY304-PIV, Nd:YLF laser; triggering rate up to 727 Hz for double frames) was used to capture the flow in the (x, y) plane in the gap and behind the downstream cylinder. The cylinder surface was painted black to minimize the laser reflection noise. The flow was seeded by smoke particles, generated from paraffin oil using a TSI 9307-6 fog generator, with a particle size of approximately 1 μm in diameter. Flow illumination was provided by two pulsed laser sources of a 527 nm wavelength, each with a maximum energy output of 30 mJ per pulse. One charge-coupled device camera (PhantomV641, double frames) was used to capture particle images with a resolution of 2560 × 1600 pixels. The laser pulse and image taking were synchronized via a Dantec timer box 80N77. A total of 1600 images were captured at the trigger rate (on the double frame mode)

of 300 Hz for each combination of d/D, L/d and U_r examined. In processing images, the interrogation window was chosen to be 32×32 pixels with a 50 % overlap in each direction. Moving-average validation then followed, where the averaging area consisted of 3×3 interrogation windows with an acceptance factor of 0.1.

The pressure signal $P(t)$ around the downstream cylinder surface was captured using a piezoresistive pressure scanner (Pressure Systems DTC Initium+ESP-32HD) with a range of ± 2.5 kPa. A total of 30 pressure taps of 0.8 mm in diameter were made around the cylinder. Adjacent taps were spanwise offset by 1 mm to minimize their possible interference, producing a spiral tap distribution with a spanwise separation of 30 mm between the first and last taps, which corresponded to the same azimuthal position and hence measured the same pressure. The 30 taps were connected to 30 ports of the pressure scanner, and the remaining two ports were connected to a Pitot tube placed upstream at $(x, y, z) = (-600$ mm, 300 mm, 0) to monitor the static pressure P_s and total pressure, based on which U_∞ may be determined. The scanner output was calibrated to give a reading of 6.22 V for the applied pressure of 1 kPa. The pressure scanner responded to the pressure fluctuation of up to 625 Hz. The ensuing phase lag is negligibly small. It is worth pointing out that the cylinder mass ratio was $m^* = 350$ for pressure measurement; and ζ and f_n were from 0.0021 to 0.043 and from 11.72 to 10.23 Hz, respectively. Consequently, U_r increases, given the same galloping vibration amplitude as that without the cables.

The pressure coefficient is calculated by $C_P(t) = (P(t) - P_s)/(0.5\rho U_\infty^2)$. The time-dependent lift force coefficient (C_L) on the cylinder is obtained by integrating the surface pressure, *viz.*

$$C_L(t) = \frac{1}{2}\int_0^{2\pi} C_p(t)\sin\theta \,\mathrm{d}\theta = \frac{1}{2}\sum_{i=1}^{i=30} C_{pi}(t)\sin\theta_i \,\Delta\theta_i, \tag{2.1}$$

where θ is the azimuthal position of a pressure tap, measured in radians from the nominal leading stagnation point of the cylinder, and i $(= 1, 2, \ldots, 30)$ indicates the pressure tap number.

3. Results and discussion

3.1. *Dependence of downstream cylinder vibration on L/d and d/D*

The maximum amplitude A of the cylinder displacement signal Y is obtained by multiplying the root-mean-square (r.m.s.) value of Y by $\sqrt{2}$, i.e. $A = Y_{rms} \times \sqrt{2}$, which provides the average amplitude of the cylinder oscillation. Figure 3 presents the dependence of A/D on d/D and L/d. At $L/d = 1.0$ (figure 3*a*), a violent vibration starts to occur at $U_r = 11.5$, 8.8, 8.0 and 7.5 for $d/D = 0.2$, 0.4, 0.6 and 0.8, respectively, but not for $d/D = 1.0$. Here, 'violent vibration' means a vibration of much larger amplitude than that in VE. A tiny hump that occurs around $U_r = 5$ is the signature of VE, and the corresponding A/D is in general less than 0.05 or 2 mm in A (figure 3*a*). At $L/d = 1.5$–2.5 (figure 3*b–d*), a violent vibration occurs for $d/D = 0.2$, 0.4 and 0.6, but not for $d/D = 0.8$–1.0. The violent vibration is evident only for $d/D = 0.2$–0.4 as L/d is increased to 3.0–4.0 (figure 3*e–g*). A further increase in L/d to 5.5 results in violent vibration only for $d/D = 0.2$ (figure 3*h*). Clearly, as L/d increases, the violent vibration takes place at smaller d/D.

Note that there is no violent vibration generated given $d/D = 1.0$ for the U_r range examined, except for a tiny hump at $U_r \approx 5$ in A/D for $L/d > 3.0$ (figure 3*f–h*)

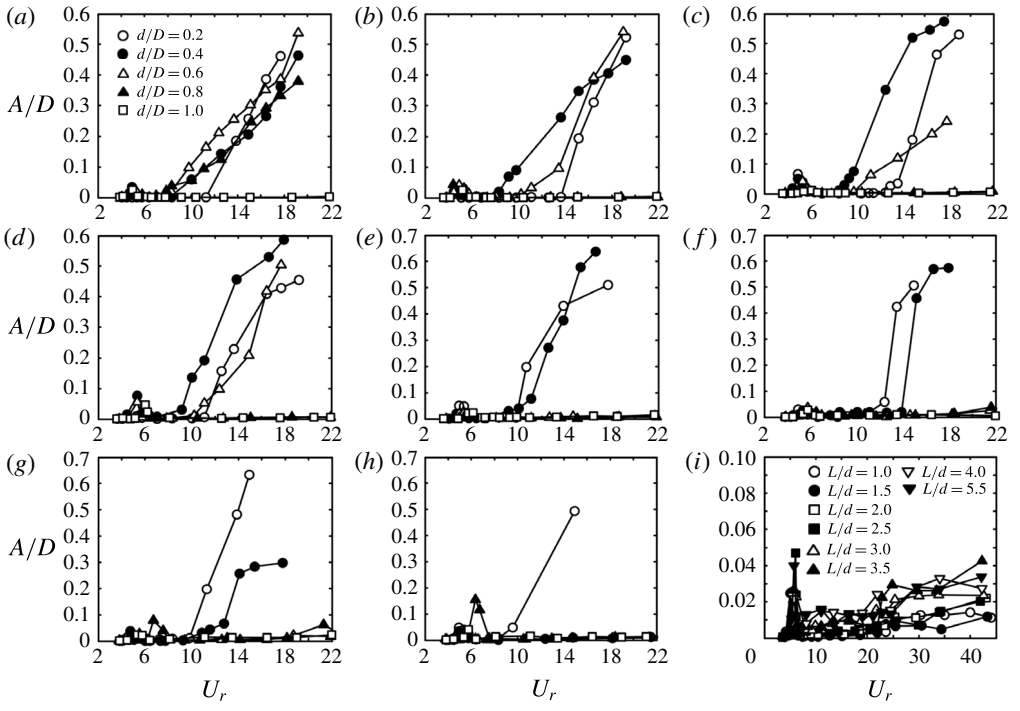

FIGURE 3. Dependence of A/D on U_r for various d/D at (*a*) $L/d = 1.0$, (*b*) 1.5, (*c*) 2.0, (*d*) 2.5, (*e*) 3.0, (*f*) 3.5, (*g*) 4.0 and (*h*) 5.5, and (*i*) for various L/d at $d/D = 1.0$. The symbols in (*i*) have the same definitions as in (*a–h*).

apparently due to vortex shedding in the co-shedding regime. Figure 3(*i*) presents the data for $d/D = 1.0$ and $L/d = 1.0$–5.5 over $U_r = 3.8$–44. The VE occurs at $U_r \approx 5$ and disappears beyond $U_r \approx 6.4$. Given $d/D = 1$, Bokaian & Geoola (1984*a*), however, observed the combined VE and galloping at $L/d = 1.0$ and separated VE and galloping at $1.5 < L/d < 2.5$. The difference can be attributed to their much smaller $m^*\zeta$ $(= 0.109)$ and Re $(= 800$–$5800)$ than the present values ($m^*\zeta = 0.58$, $Re = 4800$–$55\,000$, corresponding to $U_r = 3.8$–44.0 in figure 3*i*). Assi (2014) investigated the downstream cylinder vibration in a two-tandem-cylinder wake for $d/D = 1.0$, 0.5 and 0.33 at $L/d = 3.5$, 7.0 and 6.5, respectively, all in the co-shedding regime ($Re = 1500$–$23\,000$ or $U_r = 2$–30); their $m^*\zeta$ values were 0.0091, 0.0091 and 0.0041, respectively. Again, combined VE and galloping vibrations were observed for all three cases examined. Presently, $m^*\zeta = 0.58$ is much higher, producing quite different results, i.e. no vibration in the co-shedding regime. Note that, since $m^*\zeta$ was very small in both Bokaian & Geoola's (1984*a*) and Assi's (2014) investigations, galloping could not be separated from VE, and VE provided an initial displacement for the galloping to meet the criteria that an initial displacement is needed to trigger the gap flow switch (Zdravkovich 1974; Ruscheweyh & Dielen 1992; Dielen & Ruscheweyh 1995). The vibration amplitude in the VE regime contracts exponentially with increasing $m^*\zeta$ (Khalak & Williamson 1997). Because of the present large $m^*\zeta$, the combined VE and galloping vibration fails to occur, as is evident from the tiny hump at $U_r \approx 5$ in A/D (figure 3). Zhao & Yan (2013) numerically examined the two-degree-of-freedom vibration of two rigidly coupled

cylinders at $Re = 250$ ($m^* = 2$, $\zeta = 0$, $d/D = 0.2$, and $L/d = 0.5$ and 1.5). The VE only was observed at $L/d = 0.5$ and 1.5. Huang & Sworn (2011) investigated the hydrodynamic interaction between one pair of elastically supported rigid cylinders ($d/D = 2$ and $m^*\zeta = 0.02$). The upstream cylinder diameter was larger than that of the downstream cylinder. The Re was in the range of 16 000–72 000, corresponding to $U_r = 2$–9, which covered only the typical VE regime. The downstream cylinder vibration amplitude during VE was smaller than that of the upstream cylinder, and no galloping was observed. Owing to the presently much larger $m^*\zeta$ than others (Bokaian & Geoola 1984*a*; Assi 2014), galloping does not occur for $d/D = 1.0$ in the tandem arrangement. The galloping vibration is, however, expected even at a large $m^*\zeta$ if the downstream cylinder is placed at a lateral distance from the wake centreline (Zdravkovich 1974; Ruscheweyh & Dielen 1992; Dielen & Ruscheweyh 1995).

In the case of the downstream cylinder vibrating in the wake of an upstream cylinder, there is a need to clarify terminologies used in the literature, such as 'interference galloping' (Ruscheweyh & Dielen 1992; Dielen & Ruscheweyh 1995), 'wake galloping' (Brika & Laneville 1999), 'wake-induced galloping' (Bokaian & Geoola 1984*a*) or 'wake-induced vibration' (Assi *et al.* 2010). The interference galloping has been explained as the 'flow switching' (Ruscheweyh & Dielen 1992; Dielen & Ruscheweyh 1995). Brika & Laneville (1999) found in the wake of two tandem cylinders ($L/d = 6.5$ and 8) that the downstream cylinder exhibited a combination of VE and wake galloping, and the mechanism of the wake galloping was not elucidated. Bokaian & Geoola (1984*a*) stated that, though the excitation mechanism of wake-excited galloping is similar to that of galloping of sharp-edged bodies, an initial displacement might be required to trigger the vibration for the former. Assi *et al.* (2010) did not agree with the opinion that the excitation mechanism was similar to that of classical galloping. They proposed that the wake-induced vibration was essentially one type of vortex-induced vibration mechanisms in the sense that this vibration required an interaction between the structure and vortices from the upstream cylinder, which is different from the interactions between the shear layers and the downstream cylinder in this paper.

3.2. *Dependence of vortex shedding frequencies on L/d and d/D*

Figure 4 shows the variation in f_v/f_n with U_r for various d/D and L/d, where f_v is extracted from the power spectral density function of the HT2 signal. The Strouhal number St ($= 0.2$) in the wake of an isolated cylinder is also given as a reference. The two cylinders, when vibrating little such as at $d/D = 1.0$, may be considered to be fixed, and f_v/f_n rises with U_r, but not exactly linearly, suggesting a dependence of St on Re (Xu & Zhou 2004; Alam 2014). At $L/d = 1.0$–2.5 and $d/D = 1.0$, f_v/f_n shows a departure from $St = 0.2$ with increasing U_r or Re. The St estimated from f_v after the lock-in at which f_v is locked on with f_n ($U_r > 5$ and $Re > 6.3 \times 10^3$) drops from 0.17–0.20 to 0.14–0.15 as Re is increased from 6.3×10^3 ($U_r = 5$) to 2.8×10^4 ($U_r = 22$). The same observation of St was made by Xu & Zhou (2004) at $Re = (6\text{–}8) \times 10^3$ for two fixed tandem cylinders ($d/D = 1$) at $L/d = 1.5$–2.5 where the shear layers separated from the upstream cylinder reattached on the upstream side of the downstream cylinder. The drop in St was attributed to an upstream shift in reattachment with increasing Re. At $d/D = 1.0$ and $L/d = 3.0$ (figure 4*e*), only one f_v/f_n or $St \approx 0.13$ is detected for $U_r < 8.3$ ($Re < 1.05 \times 10^4$) but two (black and red squares) or $St \approx 0.13$ and 0.17 for $U_r \geqslant 8.3$ ($Re \geqslant 1.05 \times 10^4$). The two distinct

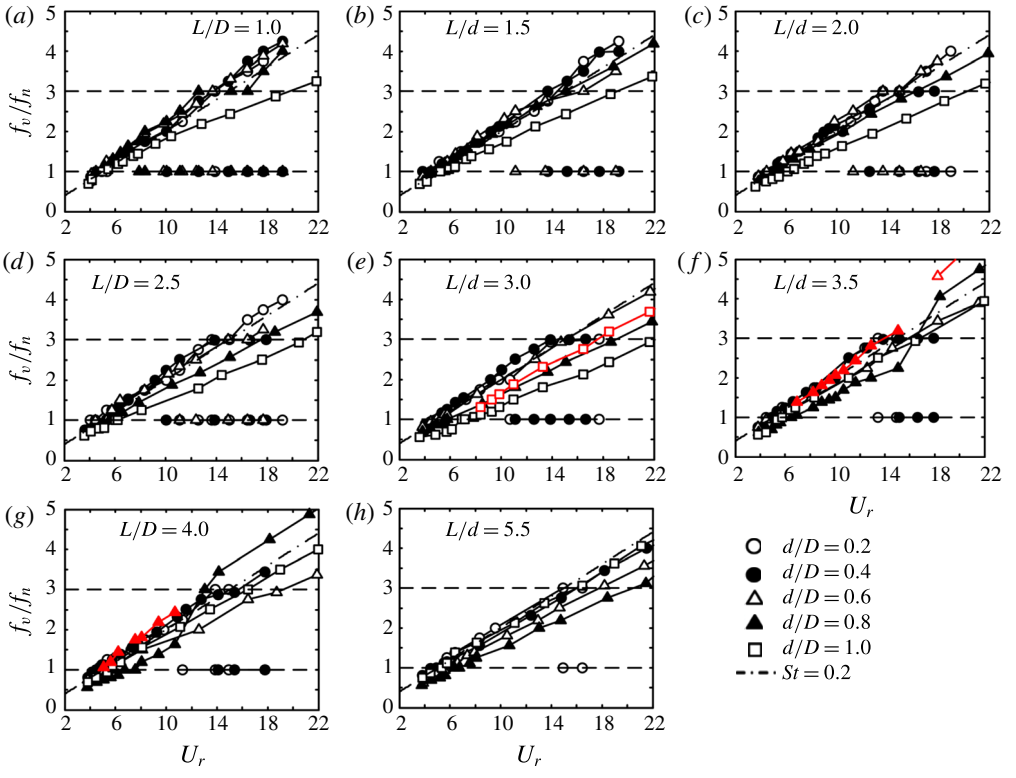

FIGURE 4. (Colour online) Variation in f_v/f_n with U_r. The two f_v/f_n values in the bistable flow are represented by the same symbols but different colours (red and black).

f_v/f_n result from the well-known bistable phenomenon or the intermittent occurrence of the reattachment and co-shedding flows, corresponding to the lower and higher f_v/f_n, respectively (Alam 2014). The latter f_v/f_n (red squares) is close to $St = 0.2$, the same as in an isolated cylinder wake, following almost a straight line with the variation in U_r, while the other (black squares) does not follow a straight line. The observation implies that St is more sensitive to a variation in Re in the reattachment regime than in the co-shedding regime. This is reasonable. A change in Re may influence the shear layer reattachment position and hence St. Igarashi (1984), Xu & Zhou (2004), Zhou *et al.* (2009) and Alam (2014) showed in the wake of two fixed cylinders that St and forces in the reattachment regime are dependent on Re as the shear layer reattachment position is sensitive to Re. For example, St is reduced when the shear layer reattachment proceeds towards the forward stagnation point (Igarashi 1984; Zhou *et al.* 2009). In the wake of two fixed cylinders ($L/d = 3.0$), Xu & Zhou (2004) observed the bistable flow at $Re = 1.5 \times 10^4$ but not at $Re \geqslant 2.0 \times 10^4$. Their Re is small compared to the present $Re > 1.05 \times 10^4$ ($U_r > 8.3$). The difference may come from the downstream cylinder vibrating at small amplitude (figure 3*i*). Flexibly supported, the downstream cylinder can be more adaptable to any change in the gap flow between the cylinders. At $L/d = 4.0$ and 5.5, where co-shedding occurs, f_v/f_n follows a straight line, consistent with the fact that the Re effect on St is insignificant in the co-shedding regime (Xu & Zhou 2004).

Two f_v/f_n are detected once the downstream cylinder is under violent vibration. The two frequencies are, however, different from those associated with the bistable flow.

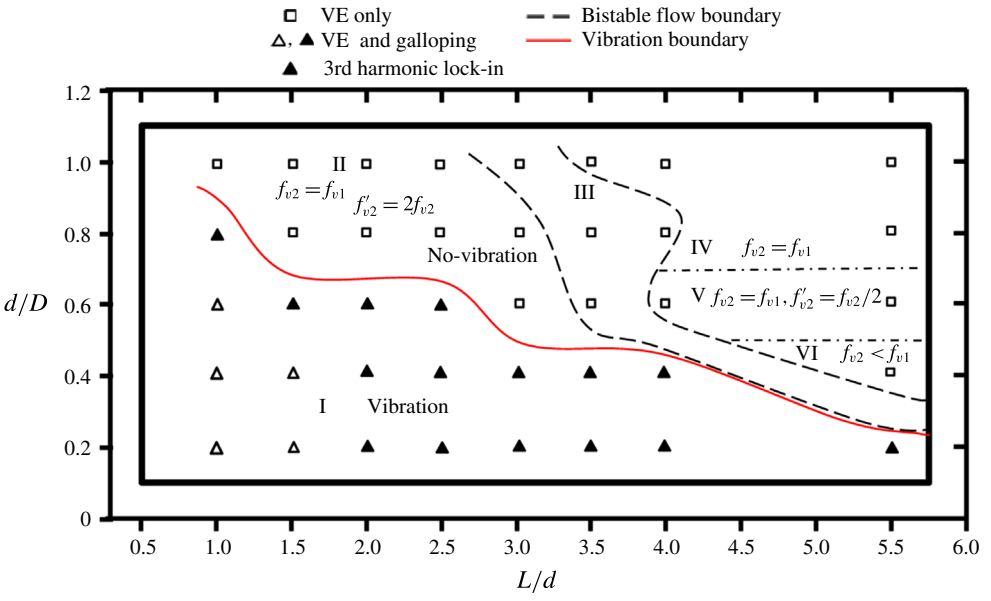

FIGURE 5. (Colour online) Vibration and flow regimes in the d/D–L/d plane ($L/d =$ 1.0–5.5, $d/D = 0.2$–1.0).

One f_v/f_n equals 1 and the other exceeds 1, increasing with U_r, which are ascribed to the cylinder vibration and natural vortex shedding, respectively. A small-amplitude vibration occurs around $U_r = 5$–7, due to VE, with $f_v/f_n \approx 1.0$.

There are a number of interesting aspects on f_v/f_n in figure 4. Firstly, f_v/f_n is closer to $St = 0.2$ for small d/D (= 0.2 and 0.4) than for large d/D, implying that, the smaller the upstream cylinder, the less is its influence on f_v and the fluctuating lift force on the downstream cylinder. The difference between the f_v/f_n value and the line of $St = 0.2$ grows for a large d/D, indicating that, the larger the d/D, the greater is the influence on flow. Secondly, it is noteworthy that f_v can be locked on to the third harmonics of f_n ($f_v/f_n = 3.0$), e.g. at $L/d = 1.0$ and $d/D = 0.8$ over $U_r = 12.6$–16.4 (figure 4*a*) and $L/d = 2.0$ and $d/D = 0.4$ over $U_r = 14$–18 (figure 4*c*). Thirdly, two distinct f_v/f_n (represented by the same symbol of different colours, red and black) occur in the bistable flow regime, i.e. at $L/d = 3.0$ and $d/D = 1.0$ over $U_r > 8.3$ (figure 4*e*), $L/d = 3.5$ and $d/D = 0.8$ over $U_r = 6.5$–15 (figure 4*f*), $L/d = 3.5$ and $d/D = 0.6$ over $U_r > 18$ (figure 4*f*), and $L/d = 4$ and $d/D = 0.8$ over $U_r = 5$–11 (figure 4*g*). While the smaller f_v/f_n value is connected to the reattachment flow, the other is associated with the upstream-cylinder-generated vortices.

3.3. *Classification of structural vibration and flow structure*

Figure 5 presents the dependence of the structural vibration, shedding frequencies and flow structure on d/D and L/d. Regime I under the solid red curve represents the occurrence of a violent vibration, largely induced by the upstream-cylinder-generated shear layer reattachment on and switch from one side to the other of the downstream cylinder. Evidently, the lock-on of the third harmonic of f_n tends to occur near the border between the vibration and no-vibration regimes. When the cylinder experiences a violent vibration, the upstream-cylinder-generated shear layers switch

their reattachment on one side to the other of the downstream cylinder, thus resulting in the lock-on at the third harmonic of f_n. The no-vibration regime can be further divided into five subregimes (II–VI) depending on the relationship between shedding frequencies f_{v1} and f_{v2} between and behind the cylinders detected by HT1 and HT2, respectively. In this paper, 'no vibration' means the absence of galloping during VE (synchronization). Regime II ($d/D > 0.8$–0.4, $L/d < 3.0$–3.5) corresponds to reattachment flow, where $f_{v2} = f_{v1}$ and a superharmonic frequency $f'_{v2} = 2f_{v2}$ (second harmonic) prevails behind the downstream cylinder. Zhou *et al.* (2009) and Xu & Zhou (2004) made extensive hot-wire measurements on two fixed identical cylinders and observed the second harmonic frequency ($f'_{v2} = 2f_{v2}$) behind the downstream cylinder in the reattachment regime. Alam *et al.* (2003) and Alam & Sakamoto (2005) also detected the second as well as the third harmonic frequency from the power spectra of fluctuating lift force ($d/D = 1$), depending on L/d. Alam (2014) noted that the third harmonic frequency occurred if the shear layer separated from the upstream cylinder reattached on the opposite side of the downstream cylinder. On the other hand, the second harmonic frequency might prevail if the shear layer reattaches on the same side of the downstream cylinder. This explains why $f'_{v2} = 2f_{v2}$ appears in regime II where the cylinder vibrates little. The bistable flow or regime III appears at a larger L/d for a smaller d/D. Regimes IV ($d/D \geqslant 0.8$, $L/d > 3.5$–4.0), V ($0.6 \leqslant d/D < 0.8$, $L/d > 4.0$) and VI ($d/D < 0.6$, $L/d > 4.0$) are connected to the co-shedding flow, characterized by synchronized ($f_{v2} = f_{v1}$), synchronized and subharmonic synchronized ($f_{v2} = f_{v1}$, $f'_{v2} = f_{v2}/2$), and non-synchronized ($f_{v2} \neq f_{v1}$) sheddings from the two cylinders, respectively. A detailed investigation of *St*, forces and flow structures in the wake of two fixed tandem cylinders with $d/D = 0.24$–1.0 was reported by Alam & Zhou (2008) in the co-shedding regime ($L/d = 5.5$) where the upstream-cylinder-generated alternate vortices impinge upon the downstream cylinder. The impingement acted essentially as a quasi-periodic excitation that is strong for $d/D \geqslant 0.4$ and weak for $d/D < 0.4$. The strong excitation forced vortex shedding from the downstream cylinder to be synchronized with that from the upstream cylinder, i.e. $f_{v2} = f_{v1}$, and the weak excitation allowed the downstream cylinder to shed vortices at a lower frequency than the upstream cylinder ($f_{v2} < f_{v1}$). Presently, synchronization is not observed for $d/D < 0.6$ as the downstream cylinder is flexibly supported.

3.3.1. *Bistable flow regime*

The bistable flow phenomenon associated with the intermittent occurrence of reattachment and co-shedding flows has been reported for two rigid cylinders (e.g. Igarashi 1982). We discuss here the bistable flow when the downstream cylinder is flexibly supported.

Figure 6 presents E_{u1}, E_{u2} and E_Y of simultaneously captured u_1, u_2 and Y signals ($L/d = 3.0$, $d/D = 1.0$ and $U_r = 11.0$). The plot of E_{u1} (figure 6*a*) displays one pronounced peak at 22.0 Hz or $St = 0.171$, while that of E_{u2} (figure 6*b*) shows two at 17.6 Hz ($St = 0.137$) and 22.0 Hz ($St = 0.171$). Obviously, the single *St* in the gap corresponds to the co-shedding mode. Under the reattachment flow mode, there should be no discernible peak in the spectra measured between the cylinders (e.g. Alam *et al.* 2003; Xu & Zhou 2004). The occurrence of two predominant frequencies is ascribed to vortex shedding from the downstream cylinder under the flow modes of reattachment and co-shedding, respectively, or the bistable flow. The plot of E_Y (figure 6*c*) shows one pronounced peak at f_n (= 11.7 Hz) and also two minor peaks at the shedding frequencies of 17.6 Hz and 22.0 Hz.

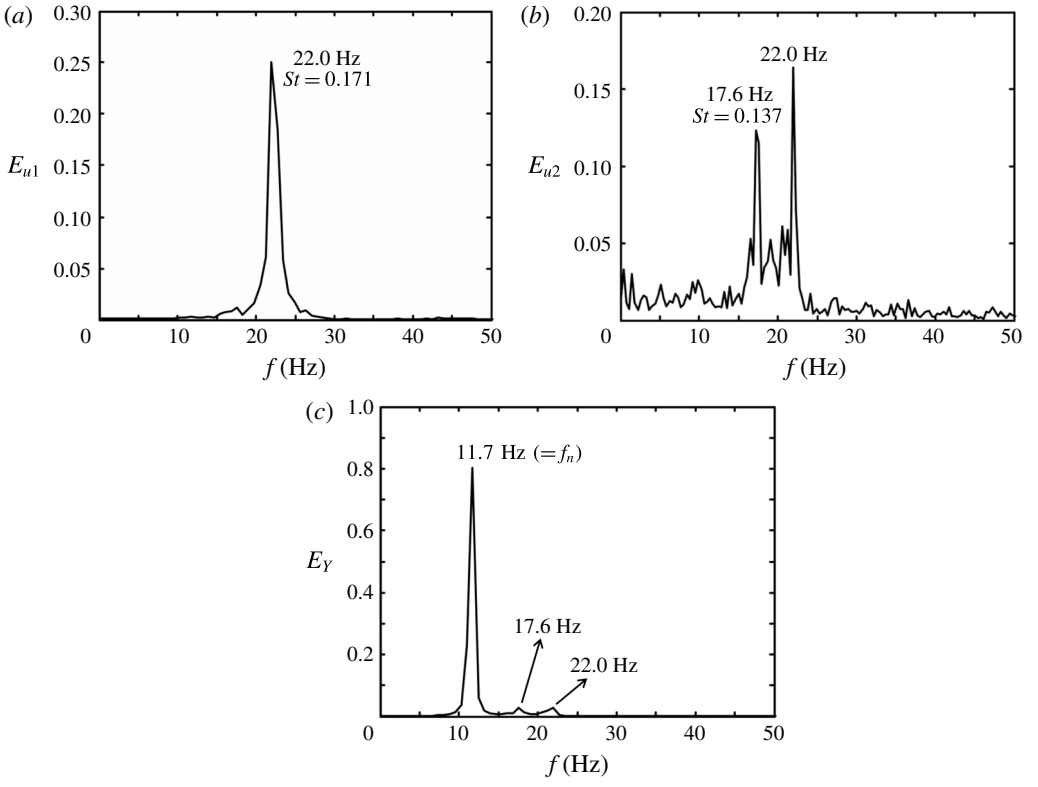

FIGURE 6. (*a–c*) Power spectral density functions E_{u1}, E_{u2} and E_Y of simultaneously captured u_1, u_2 and Y, respectively.

3.3.2. *Violent vibration regime*

In view of the objectives of this work, we present first data showing the dependence of the vibration response on d/D and L/d and thus classify the flow regimes with and without vibration. To understand the initiation and mechanism of the vibration, we illustrate one representative case, i.e. $L/d = 2.0$ and $d/D = 0.4$, which occurs near the centre of the vibration regime in the L/d–d/D plane. It is worth pointing out that we have actually examined a number of other cases, which are not shown because of the same flow physics.

3.3.2.1. *Connection between vibration and vortex shedding*. Representative E_{u2} and E_Y ($d/D = 0.4$, $L/d = 2.0$) are shown in figure 7(*a*,*b*). The $f/f_n = f_v/f_n$ corresponding to the peaks in the spectra (figure 7*a*) depends on U_r, as shown in figure 7(*c*). The corresponding vibration response is given in figure 7(*d*). Figure 7 allows us to identify the sources of structural vibration, as indicated on the left side of figure 7(*a*). A small peak that occurs over $U_r = 4.5$–5.3 in figure 7(*d*) corresponds to $f_v/f_n = 1.0$ in both E_{u2} and E_Y (figure 7*a*,*b*), apparently due to the lock-in of vortex shedding with the first-mode structural vibration or the resonance. At $U_r = 3.8$, one peak only occurs at $f/f_n = 0.875$ in figure 7(*a*) and two at $f/f_n = 0.875$ and 1.0 in figure 7(*b*), implying that f_v is not locked in with f_n. Naturally, the cylinder vibration is insignificant or negligibly small at both f_v and f_n. At $U_r = 5.3$, again two peaks are observed at $f/f_n = 1.0$ and 1.19 in figure 7(*a*,*b*). The peak at $f/f_n = 1.0$ is less pronounced in E_{u2}

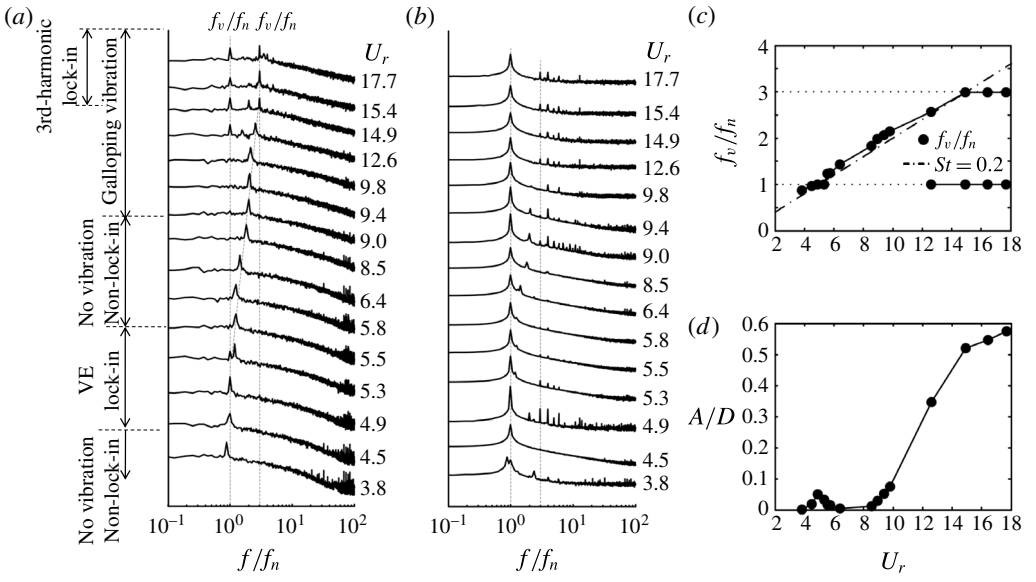

FIGURE 7. Power spectral density functions (*a*) E_{u2} and (*b*) E_Y, and dependence on U_r of (*c*) f_v/f_n, and (*d*) A/D, for $L/d = 2.0$ and $d/D = 0.4$.

and more in E_Y than its counterpart at $f/f_n = 1.19$, suggesting an intermittent lock-in in the transition between the lock-in (VE) and non-lock-in. The peak at $f/f_n = 1.0$ indicates the occurrence of lock-in and the other at $f/f_n = 1.19$ corresponds to natural vortex shedding. The intermittent lock-in at the boundary between the lock-in and non-lock-in regimes is a well-established phenomenon (Leontini *et al.* 2006). For a single circular cylinder, Pan, Cui & Miao (2007) found that C_L and Y/D appeared less periodic at the end of the lock-in range due to the intermittent occurrence of lock-in.

As U_r goes beyond the lock-in range (figure 7*a*,*c*), $f_v/f_n \neq 1.0$, rising monotonically following $St = 0.2$ until $U_r = 8.5$. There is little vibration over $5.3 < U_r < 8.5$. Similarly to the non-lock-in at $U_r = 3.8$, one and two peaks are seen in E_{u2} and E_Y, respectively. The A/D value becomes quite significant at $8.5 \leqslant U_r < 9.8$ (figure 7*d*); the second peak corresponding to f_v is more appreciable (figure 7*b*), though E_{u2} does not show any peak at $f_v/f_n = 1.0$ (figure 7*a*). The results indicate that the vibration is initiated by vortex shedding from the cylinder, not due to excitation at f_n. More evidence will be provided later. On the other hand, when A/D is large enough at $U_r > 9.8$, E_{u2} display two prominent peaks (figure 7*a*), corresponding to $f_v/f_n = 1.0$ and $St = 0.2$ (figure 7*c*). The latter is maintained up to $U_r = 14.9$ and then f_v is locked in with the third harmonic of f_n for $U_r > 14.9$, where A/D rises slowly.

3.3.2.2. *Downstream cylinder vibration effect on flow.* The flows at $U_r = 4.9$ and $U_r = 14.9$ are examined to understand the differences between the flow structures associated with the VE and galloping vibrations. For each U_r, using the Y signal as a reference signal, we calculated the phase-averaged vorticity contours, based on 64 images, at eight instants for each period T of the cylinder oscillation. The contours of the eight instants are presented for $U_r = 4.9$ in figure 8(*a–h*). The correspondence between time instant and cylinder displacement is given in figure 8(*i*). Here $t/T = 0$ refers to the

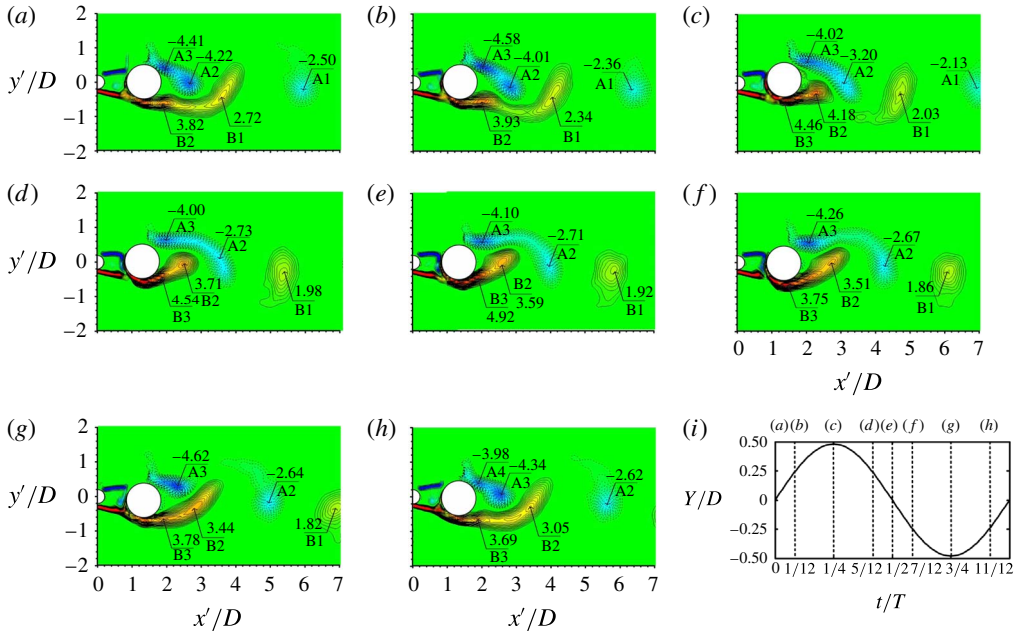

FIGURE 8. (Colour online) (*a–h*) Phase-average vorticity ω_z^* $(= \omega_z D/U_\infty)$ contours in one vibration cycle. Solid and dotted contour lines stand for clockwise and anticlockwise vorticities. The contour cut-off levels are ± 0.2 and the increment is 0.2. (*i*) Variation in Y/D with t/T where the time instants are specified by the dashed lines corresponding to (*a–h*). Here $L/d = 2.0$, $d/D = 0.4$ and $U_r = 4.9$.

instant when the cylinder crosses the equilibrium position $Y/D = 0$, moving upwards. The vortex formation process may be divided into three stages: growth, saturation and decay (Jeon & Gharib 2004). The three stages are also seen presently when the downstream cylinder is vibrating, as discussed below.

VE vibration. Under the VE vibration ($U_r = 4.9$), the lower shear layer in the gap at $t/T = 0$ reattaches onto the lower front side of the downstream cylinder and splits into two (figure 8*a*). One moves downstream, and the other flows over the front surface and meets the upper shear layer streaming on the upper side of the downstream cylinder. Four vortices, i.e. B1, B2, A2 and A3, are separated from the downstream cylinder. Between the instants in figure 8(*a*) and figure 8(*b*), B2 and A3 are close to the flow separation point and grow due to the continued addition of vorticity from the boundary layers. At the instant in figure 8(*b*), B1 is about to separate to become a free vortex (Gerrard 1966). As Y/D reaches its maximum (figure 8*c*, $t/T = 1/4$), the upper shear layer in the gap reattaches, and part of the reattached shear layer flows along the lower side of the cylinder (figure 8*c*). B1 is now completely separated with a tail. Between $t/T = 1/12$ and $1/4$, B2 moves downstream appreciably, but A3 does not, indicating vortex shedding from the lower side. Consequently, a new vortex B3 emerges on the lower side (figure 8*c*,*d*). Being closer to the separation point than B2, B3 accumulates vorticity and grows during $t/T = 1/4$–$5/12$. Since vortex shedding from the lower side takes place during the half period (figure 8*a–e*), A3 is not advected downstream appreciably.

As the cylinder crosses $Y/D = 0$ and moves downwards, vortex shedding from the upper side starts to occur. A3 moves downstream and grows during $t/T = 1/2$–$3/4$.

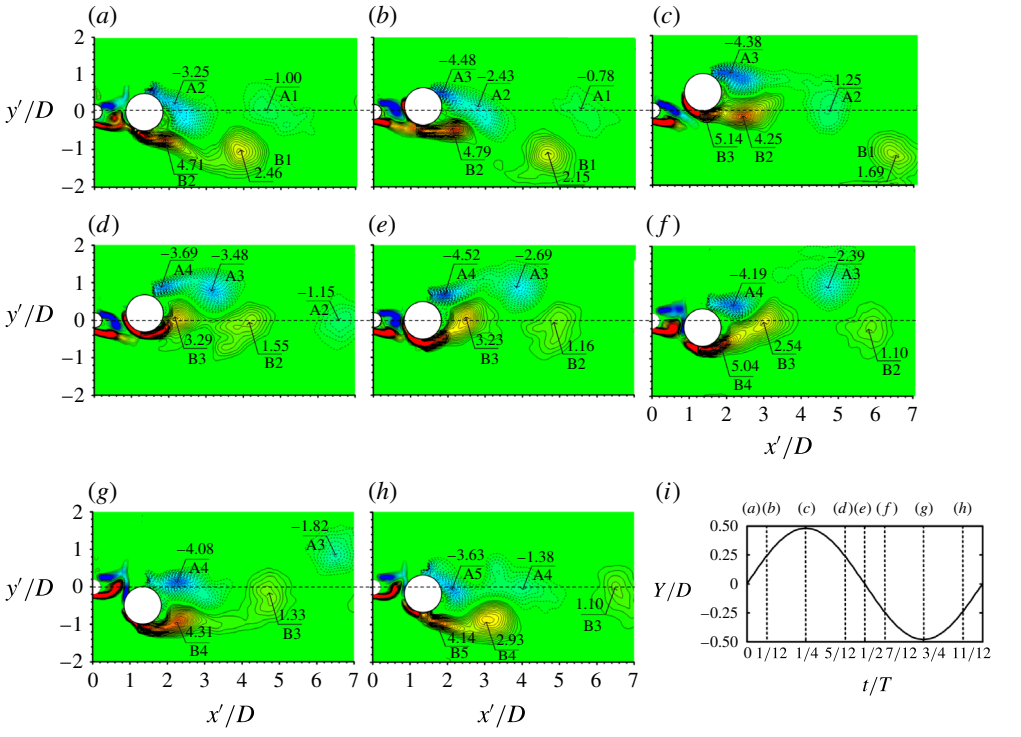

FIGURE 9. (Colour online) (*a–h*) Phase-average vorticity $\omega_z^* \ (=\omega_z D/U_\infty)$ contours in one cycle. Solid and dotted contour lines stand for clockwise and anticlockwise vorticities. The contour cut-off levels are ± 0.2 and the increment is 0.2. (*i*) Variation in Y/D with t/T where the time instants are specified by the dashed lines corresponding to (*a–h*). Here $L/d = 2.0$, $d/D = 0.4$, $A/D = 0.48$ and $U_r = 14.9$.

A new vortex A4 emerges at $t/T = 11/12$. The lower shear layer reattaches again at $t/T = 3/4$, and A2 is detached with a tail from the shear layer. It may be inferred that vortex shedding occurs largely from the lower side for $Y/D > 0$ and from the upper side for $Y/D < 0$. Therefore, in each oscillation cycle, two free vortices B1 and A2 are completely separated from the shear layers (figure 8*b*,*f*) and two new vortices B3 and A4 emerge. As such, the dynamics of the wake behind the vibrating cylinder is similar to what is found in a classical von Kármán street, exhibiting the classical 2S vortex formation mode (Williamson & Roshko 1988). Although the reattached shear layers sweep over the front surface of the downstream cylinder, the flow in the gap between the cylinders is mostly stagnant and the lateral positions of the gap shear layers change little during the oscillation of the downstream cylinder. The observation suggests that the shear layer separated from the upstream cylinder may not produce a significant effect on the lift and hence vibration of the downstream cylinder. Rather, the vibration is generated due to vortex shedding from the downstream cylinder.

Galloping vibration. The flow structure exhibits a difference at $U_r = 14.9$ ($L/d = 2.0$ and $d/D = 0.4$) when galloping occurs. Figure 9 presents the phase-averaged vorticity contours during one cycle of oscillation. Recall that the third harmonics lock-in occurs at $U_r = 14.9$–17.7 for $L/d = 2.0$ and $d/D = 0.4$. The corresponding flow structure will be explored here. At $t = 0$ ($Y/D = 0$), the lower shear layer separated from the

upstream cylinder reattaches on the downstream cylinder while rolling up in the gap, a small part of the reattached flow joining the lower shear layer of the downstream cylinder (figure 9*a*). As the cylinder moves upwards, the upper gap shear layer reattaches on the cylinder (figure 9*b*) and swerves downwards without reattachment when Y/D is large enough (figure 9*c*). Both upper and lower gap shear layers join the lower shear layer around the downstream cylinder (figure 9*b*,*c*). Unlike A2 and B2, a new vortex A3 emerging between the instants in figure 9(*b*) and figure 9(*c*) originates from the shear layer over the upper side of the cylinder. This vortex does not seem to interact directly with the shear layers separated from the upstream cylinder. A2 occurs on the wake centreline ($y'/D = 0$) at the instant in figure 9(*c*). B2 below $y'/D = 0$ follows the cylinder movement and moves towards $y'/D = 0$ from the instant in figure 9(*a*) to figure 9(*c*). While leading B2 marginally at the instant in figure 9(*a*), A2 is $2.25D$ downstream of B2 in figure 9(*c*). Both A2 and B2 occur near $y'/D = 0$ in figure 9(*d*), and their streamwise separation remains unchanged from the instant in figure 9(*c*) to figure 9(*d*).

A3 stays away from the wake centreline during the cylinder downward motion (figure 9*c–g*). New vortices B3 and A4 emerge at the instant in figure 9(*d*), and B3 leads A4. They interact vigorously with each other (figure 9*d–f*). A4 on the upper side follows the cylinder downward motion, approaching $y'/D = 0$. In figure 9(*h*), both A4 and B3 are on $y'/D = 0$. It is interesting to note that A3 and B4 are formed from the shear layers, pushed away from the upstream cylinder wake, at the instants in figure 9(*b*,*c*) and (*f*,*g*), respectively, and both stay away (approximately $y/D = \pm 1$) from the wake centreline, not directly interacting with the gap shear layers. On the other hand, B2 and A2 originate at least partially from the gap shear layers and end up on the wake centreline. So do B3 and A4. Thus, a total of six vortices are formed during one cycle of the cylinder oscillation, accounting for the third harmonic lock-in, $f_v/f_n = 3.0$.

While vortices B2, A2, B3 and A4 near the centreline decay rapidly in terms of the maximum vorticity concentration, A3 and B4, far away from the centreline, do so rather slowly. The wake is thus dominated by the latter type of vortex produced alternately following the up-and-down cylinder oscillation. It will be shown later that the cylinder receives energy from flow (positive work) during the shedding process of the former type of vortex. On the other hand, the flow absorbs energy from the cylinder (negative work) during the shedding of the other type of vortex. This difference in energy transfer may also explain why the former type of vortex decays rapidly and the latter survives longer.

The vortex shed from the downstream cylinder swerves downwards at the instants in figure 9(*a*,*b*) when the cylinder moves upwards, vortex shedding appearing symmetric in figure 9(*c*) when the cylinder velocity is zero (maximum Y/D). As the cylinder moves downwards (figure 9*c*,*d*), the vortex shed from the downstream cylinder is deflected upwards, with a maximum deflection occurring at the instant in figure 9(*e*) when the cylinder velocity is maximum. The two gap shear layers pass over the lower and upper sides of the downstream cylinder that reaches the maximum (figure 9*c*) and minimum Y/D (figure 9*g*), respectively. Obviously, the alternating reattachment and switch of the two gap shear layers from one side to the other follow the cylinder oscillation, the switch frequency being synchronized with the cylinder oscillation frequency. Accordingly, there is a radical change in the pressure distribution around the downstream cylinder, which will be discussed in § 3.4. A smaller d/D facilitates the gap shear layer switch, as the shear layers can attach at a small incident angle. On the other hand, a large d/D leads to the occurrence of the reattachment at a

relatively large incidence angle. Thus, a small d/D is associated with a violent vibration (figure 5).

The gap flow switch has been suggested as an excitation mechanism of vibration for a flexible cylinder placed behind another of identical diameter (Zdravkovich 1988; Knisely & Kawagoe 1990; Ruscheweyh & Dielen 1992; Dielen & Ruscheweyh 1995). The downstream cylinder oscillation could not be excited if placed in line with the upstream cylinder but could be excited if given an initial displacement of greater than $0.2D$ (Zdravkovich 1974) or a flow incidence angle of more than 10°. The oscillation is generated due to the occurrence of two flow modes, one with a strong gap flow producing a large inward lift force and the other without gap flow (shear–shear layer reattachment) associated with a negligible lift force (Zdravkovich 1988; Dielen & Ruscheweyh 1995). For a stationary downstream cylinder, the former mode may take place when the lateral distance between the two cylinders and the incidence angle exceed critical values. For an elastic downstream cylinder, a strong gap flow persists longer when the downstream cylinder moves towards the wake centreline than moving away from the centreline, and the mode without gap flow starts later as the cylinder shifts away from the centreline. This means a spatial phase lag of flow switching with respect to the lateral motion of the downstream cylinder (Ruscheweyh & Dielen 1992; Dielen & Ruscheweyh 1995). As a result, a phase lag is generated between C_L and Y, which makes the vibration sustainable, corresponding to a positive energy transfer from the flow into the cylinder. Dielen & Ruscheweyh (1995) proposed the above scenario based on the data of two stationary cylinders, without any information from simultaneously measured C_L and Y/D. Their scenario is to a certain extent consistent with the present observation, explaining why the downstream vibration is excited for $d/D < 1.0$ but not for $d/D = 1.0$. While their scenario suggests only the gap flow switching, our data show unequivocally that the interaction of the two gap shear layers with the downstream cylinder plays a key role for the generation of the structural vibration.

Based on the quasi-steady theory of galloping, galloping cannot be generated for an axisymmetric body, e.g. a circular cylinder (Bearman *et al.* 1987). As such, one question arises: Why does galloping takes place for the circular cylinder placed in the wake of another? The two cylinders in tandem are connected by shear layers in the reattachment regime. Then, the effective shape of the two-cylinder system is no longer axisymmetric; hence the two cylinders may be prone to generating galloping vibrations. Given that the upstream cylinder is not fixed, galloping may also occur for the upstream cylinder in the reattachment regime (Bokaian & Geoola 1984*b*). In the co-shedding regime, the upstream cylinder does not experience galloping but the downstream cylinder does (Bokaian & Geoola 1984*a*,*b*). This is because the upstream cylinder may be considered to be isolated and is now axisymmetric. On the other hand, the downstream cylinder is not axisymmetric with respect to local approaching flow since the flow between the cylinders is non-uniform. Therefore, the galloping motion of the downstream circular cylinder, observed in both reattachment and co-shedding regimes, is not a violation of the galloping theory.

Wake evolution. The wake pattern is sketched over a longer range of x/D in figure 10 so that the vortex generation and dynamics can be better illuminated. The cylinder position corresponds to the instant in figure 9(*h*) and the vortices are shed at the instants in figure 9(*a–h*). The lateral separations from the centreline ($y/D = 0$) of vortices A3 and B1 are $y/D = \pm 1$, as discussed before. The vortices are placed in the wake based on their positions. The streamwise separations between free vortices A4 and B3, B3 and A3, and A3 and B2 are $2.4D$, $1.8D$, and $1.0D$, respectively, which are

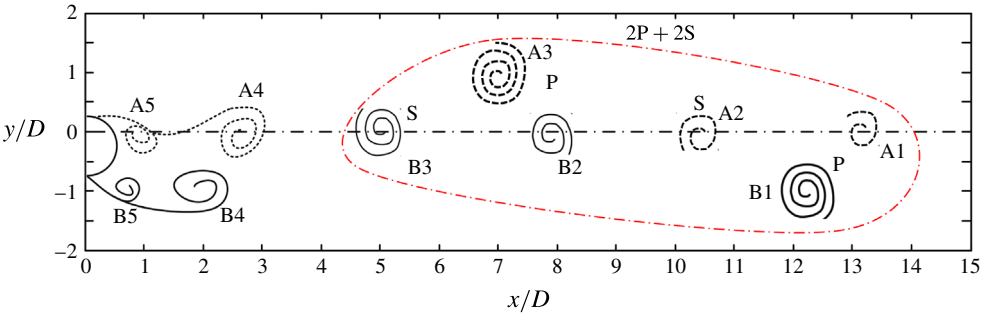

FIGURE 10. (Colour online) Sketch of the vortex street behind the cylinders, following figure 9. P and S stand for a vortex pair and a single vortex, respectively. The red dashed line encircles the vortices shed in one complete oscillation cycle.

extracted from figure 9(*h*,*g*,*f*), respectively. Also, the streamwise distances between B2 and A2, A2 and B1, and B1 and A1 are 2.4*D*, 1.8*D* and 1.0*D*, respectively, obtained from figure 9(*d*,*c*,*b*) in view of the observation that the convection velocity of vortices changes little beyond $x/D = 5.7$ (Lin & Hsieh 2003). It seems that vortices A1, B1 and A2 form one set, whilst B2, A3 and B3 form another. Interestingly, the latter set originates from the cylinder surface during the cylinder moving from the centreline to the top (figure 9*a–c*) and the associated shedding occurs during the cylinder motion from the top to the centreline. Similarly, the former set of vortices emerges in the next half cycle of the cylinder motion. The vortices on the centreline decay rapidly, as discussed earlier. Being close to each other, B2 and A3 may be considered to be one pair. Although the pattern appears like a 2P + 2S pattern, the downstream wake survives in a 2S pattern.

Figure 11 presents the instantaneous vorticity contours for one oscillation cycle of the cylinder at $U_r = 12.6$. Note that f_v/f_n at $U_r = 12.6$ is 2.6 (figure 7*c*), which is a non-integer number, that is, the downstream cylinder oscillation and vortex shedding do not have a fixed phase shift. Thus phase averaging is inappropriate. Between the instants in figure 11(*a*) and figure 11(*b*), concentration A2 tends to break away from the upper shear layer, while B2 grows in size. As the cylinder reaches its maximum amplitude (figure 11*c*), B2 breaks away and A3 grows, accompanied by A4. From figure 11(*a*) to figure 11(*c*), two vortices (A2 and B2) are formed, with vorticity originated largely from the upper shear layer, which is connected to the upward movement of the cylinder. Similarly, from figure 11(*c*) to figure 11(*g*), three vortices A3, B3 and A4 are generated, and vorticity largely originates from the lower shear layer. B4 is about to break away at the instant in figure 11(*h*) and $t/T = 1.0$ (not shown). Thus, a total of 5+ vortices are separated from the cylinder, joining the vortex street, in one period of oscillation. The result conforms to $f_v/f_n \approx 2.6$ in a 2S mode. No pairing is observed among these vortices. It is worth pointing out that another frequency at $f_v/f_n = 1.0$ is observed at $U_r = 12.6$ (figure 7*a*), which is due to the cylinder oscillation as the very near wake is directed upwards with the cylinder moving downwards and *vice versa*.

Sen & Mittal (2015) numerically studied the in-line and transverse free vibrations of a square cylinder. For $m^* = 10$ and 20, the classical galloping vibration occurred and a total of six vortices were generated within an oscillation cycle of low oscillation amplitude, forming a 3(2S) pattern. The pattern changed to 2P+2S when the transverse displacement surpassed a threshold. It may be inferred that, with an increase in U_r

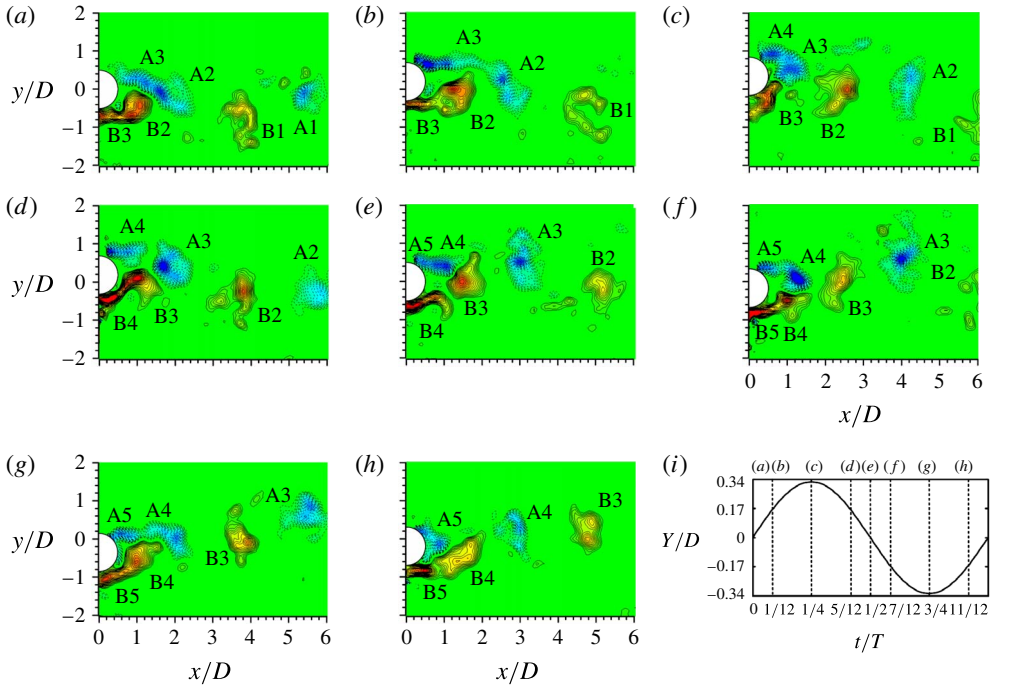

FIGURE 11. (Colour online) (*a–h*) Instantaneous vorticity ω_z^* $(= \omega_z D/U_\infty)$ contours in one vibration cycle. Solid and dotted contour lines stand for clockwise and anticlockwise vorticities. The contour cut-off levels are ± 0.6 and the increment is 0.3. (*i*) Variation in Y/D with t/T where the time instants are specified by the dashed lines corresponding to (*a–h*). Here $L/d = 2.0$, $d/D = 0.4$ and $U_r = 12.6$.

from 12.6 to 14.9, the transverse displacement of the cylinder increases and the transition from the 2S to 2P+2S pattern might take place.

In order to understand further the flow evolutions under the VE, no vibration and violent vibration, HT2 was traversed from $x/D = 4$ to 30 in the wake for three different $U_r = 4.7$ (VE), 8.3 (no vibration) and 14.9 (violent vibration). The power spectra of the HT2 signals are presented in figure 12. When the cylinder does not vibrate (figure 12*b*), the only peak at f_v in E_{u2} decays rapidly as x/D increases. On the other hand, in the VE regime, the peak is relatively wider and decays less rapidly (figure 12*a*). For the violent vibration case (figure 12*c*), the peak at $f_v/f_n = 3$ wanes rapidly with increasing x/D. However, the peak at $f/f_n = 1.0$ grows downstream. The observation is internally consistent with the finding from figure 9 that the vortices connected to shear layer impingement decay rapidly and those shed when the cylinder is far away from the centreline persist longer.

3.4. *Pressure and force on the vibrating cylinder*

In this section, interactions between the shear layer/vortex and the downstream cylinder will be discussed in terms of the phase-averaged pressure coefficient $C_{P\text{-}pa}$ (figure 13*a–e*) and lift force coefficient C_L (figure 13*f*). The $C_{P\text{-}pa}$ is positive when pointing to the cylinder centre, and a length of $D/2$ corresponds to $|C_{P\text{-}pa}| = 1.0$. The concurrent Y/D and C_L are plotted in figure 13(*f*) for one half cycle of the cylinder oscillation.

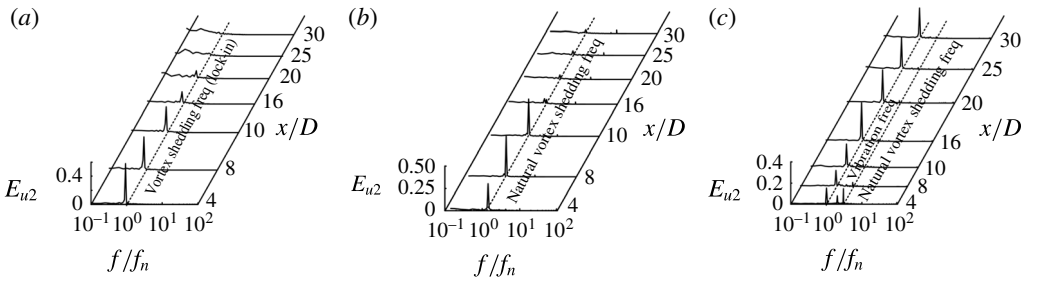

FIGURE 12. Power spectral density function E_{u2} for (a) VE at $U_r = 4.7$, (b) no vibration at $U_r = 8.3$, and (c) galloping at $U_r = 14.9$. Here $L/d = 2.0$ and $d/D = 0.4$.

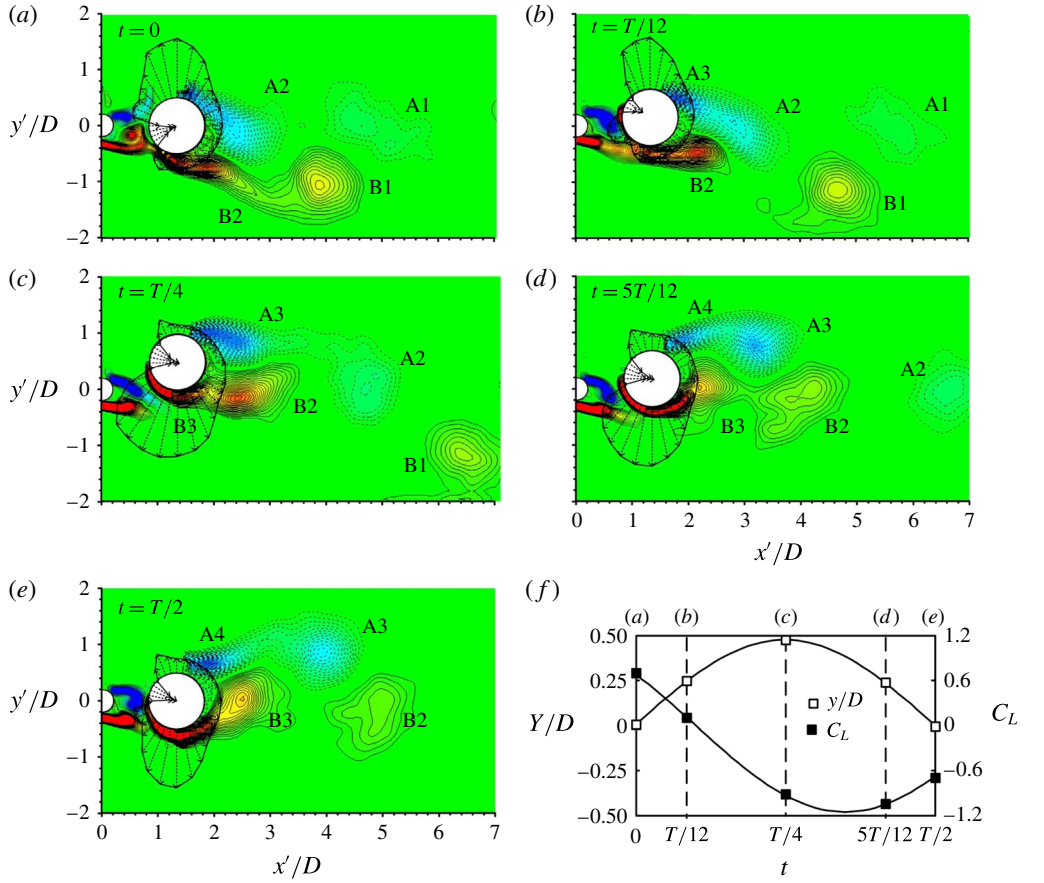

FIGURE 13. (Colour online) (a–e) Phase-averaged vorticity contours and pressure coefficient $C_{P\text{-}pa}$ around the downstream cylinder in one half cycle of the cylinder oscillation. The contour cut-off levels are ± 0.2 and the increment is 0.2. (f) Variation with time in the displacement Y/D and lift force coefficient C_L over the half cycle. Here $L/d = 2.0$, $d/D = 0.4$ and $A/D = 0.48$.

At the instant in figure 13(a), the lower gap shear layer reattaches at a small incidence angle on (almost perpendicularly to) the downstream cylinder surface at

$\theta \approx -22.5°$, where $C_{P\text{-}pa} \approx +1.0$. The high-momentum fluid of the reattached shear layer follows largely the upper surface of the downstream cylinder and joins the upper shear layer, giving rise to a highly negative pressure on the upper side and resulting in an upward lift force (figure 13*a*). At the instant in figure 13(*b*), the cylinder is away from the centreline, and the gap upper shear layer reattaches on the downstream cylinder at a large incidence angle. The maximum $C_{P\text{-}pa}$ is 0.71 at $\theta \approx 33.75°$. The lower front cylinder surface is now submerged in the wake of the upstream cylinder, resulting in a negative pressure with a maximum $C_{P\text{-}pa}$ of -0.2 at $\theta \approx -57°$. The major difference in the pressure patterns between figure 13(*a*) and figure 13(*b*) is that the positive pressure region shifts from the lower to the upper side. Thus C_L drops. There is a drastic change in the pressure distribution between the two instants; the highly negative pressure is now on the lower side of the cylinder, as a result of both upper and lower gap shear layers flowing over the lower side of the cylinder. As such, C_L drops further from the instant in figure 13(*b*) to figure 13(*c*). Interestingly, while changing greatly during the cylinder motion from the centreline to the top (figure 13*a–c*), the pressure distribution does not change much as the cylinder moves from the top to the centreline, pointing to a hysteresis.

As another interesting observation, it is the interaction between the gap shear layers and the downstream cylinder that largely causes the change during the cylinder motion in the pressure distribution over the front and side surfaces, not vortex shedding from the downstream cylinder.

The time-mean pressure on the cylinder surface, when galloping takes place, is shown in figure 14(*a*). The pressure distribution is symmetric about $\theta = 180°$, indicating a zero mean lift for each cycle, which is also reflected in the time history of C_L (figure 14*b*). As an extension of their earlier work (Sen & Mittal 2015), Sen & Mittal (2016) found at a low *Re* that during the galloping vibration the transition from the 3(2S) to 2P+2S pattern is accompanied by a transition from the quasi-periodic flow/body motion to the periodic flow/body motion. At the present high *Re*, the cylinder motion during galloping is always periodic with almost unchanged amplitude ($\pm 4\,\%$) since the galloping vibration is sustained by the gap shear layer switching, not by the classical galloping mechanism that prevails in the case of a vibrating square cylinder.

3.4.1. *Work done*

Whether a vibration is sustainable depends on the energy transfer between fluid and cylinder, which is subsequently linked to the way a vortex is shed from the cylinder. It is important to understand the work done by C_L during cylinder vibration and vortex shedding, separately. To this end, C_L is low- and high-pass-filtered at a cut-off frequency of 15 Hz. Figure 15 presents the temporal evolution of instantaneous and cumulative work, W_{fi} $(= C_L \times d(Y/D))$ and $\sum W_{fi}$ $(= \sum C_L \times d(Y/D))$, done in two cycles of oscillations, where subscripts 1 and 2 denote the low- and high-pass-filtered C_L, respectively, used in calculating W_{fi} or $\sum W_{fi}$. Thus W_{fi}, $W_{fi,1}$ and $W_{fi,2}$ represent the total work done, work done from C_L at the vibration frequency, and work done from C_L at higher frequencies, respectively. Positive and negative W_{fi} indicate flows acting to excite and to dampen the vibration, respectively.

As shown in figure 15(*a*), C_L decreases to zero as the cylinder moves upwards from $Y/D = 0$ to 0.31, resulting in positive but decreasing $W_{fi,1}$ (process A). As the cylinder continues its upward movement till the top position where $d(Y/D) = 0$, $W_{fi,1}$ becomes negative (process B). Interestingly, the gap shear layers are involved in the positive $W_{fi,1}$ and the vortices formed when the cylinder is far away from $Y/D = 0$

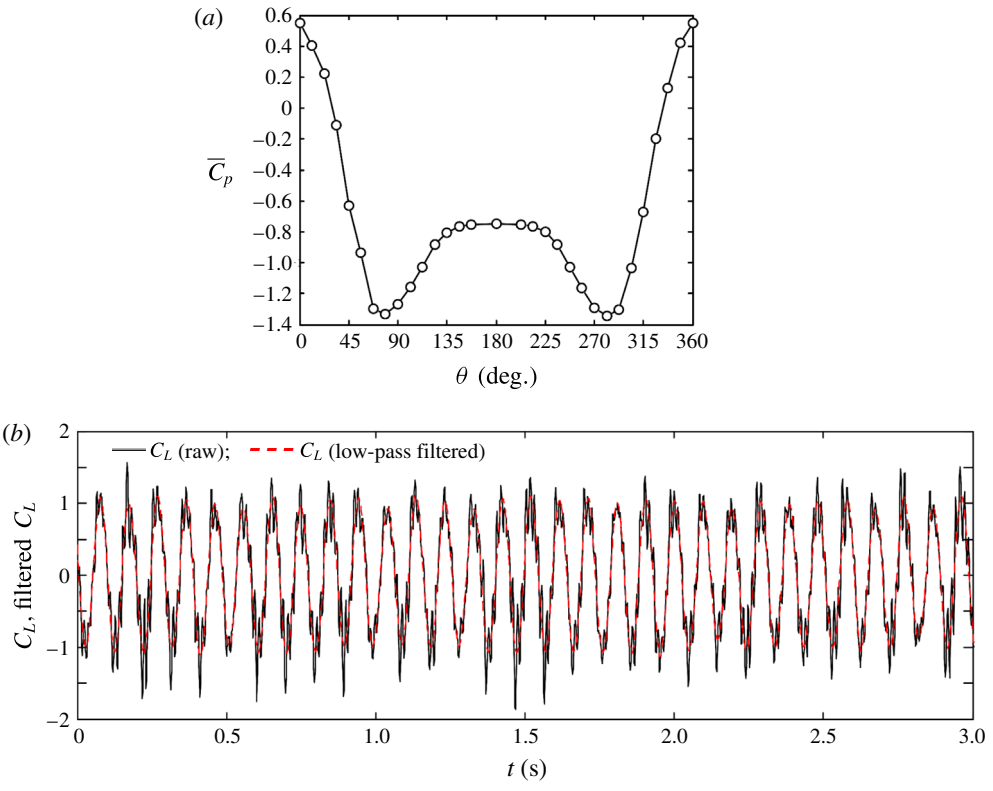

FIGURE 14. (Colour online) (*a*) Time-mean pressure coefficient distribution $\overline{C}_p$ around the cylinder. (*b*) Time histories of C_L and 20 Hz low-pass-filtered C_L. The conditions are the same as in figure 13.

are connected to the negative $W_{fi,1}$. Next, as the cylinder moves downwards from the top, $W_{fi,1}$ remains positive and reaches its maximum during this quarter of the period (process C). Evidently, there is one half cycle of oscillation in hysteresis due to a phase lag between C_L and Y/D, which results from the interaction between the shear layers, separated from the upstream cylinder, and the downstream cylinder as observed in the temporal evolution of the flow structure in figures 9 and 13. A summary sketch of the work done is presented in figure 15(*d*). While the cylinder moves upwards to $Y/D = 0.31$, the work done is positive and the cylinder absorbs energy from the flow (process A) when the shear layer reattachment takes place and switches from one mode to the other (figure 13). From $Y/D = 0.31$ to its maximum, the work done is negative and the flow receives energy from the vibrating cylinder. However, when moving from the top to $Y/D = 0$, the cylinder gains energy from the flow for the entire process C, the maximum energy transfer rate occurring at $Y/D = 0.19$. Interestingly, the energy the cylinder receives is mostly (approximately 75 % of the total energy transfer) transferred at $Y/D < 0.31$ where the gap shear layers interact vigorously with the downstream cylinder. It seems plausible that the shear layer reattachment and switch are the main sources to generate the cylinder vibration. The $\sum W_{fi,1}$ calculated from the low-pass-filtered C_L is similar to $\sum W_{fi}$ calculated from the unfiltered C_L (figure 15*b*). The $\sum W_{fi,2}$, calculated over two cycles, is very small, approximately 0.08, compared with $\sum W_{fi,1}$ (≈ 2.0). That is,

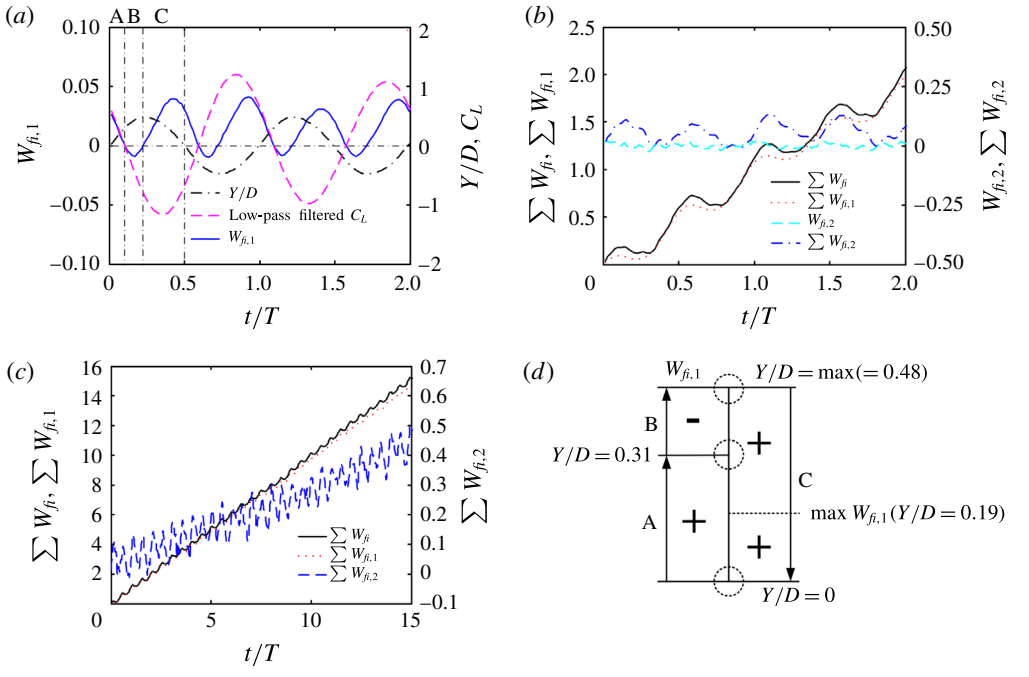

FIGURE 15. (Colour online) (*a*) Time histories of Y/D, filtered C_L and instantaneous work done W_{fi} in two cycles. (*b*,*c*) Variations in $W_{fi,2}$, $\sum W_{fi}$, $\sum W_{fi,1}$ and $\sum W_{fi,2}$ in (*b*) two cycles and (*c*) 15 cycles. (*d*) Sketch for the signs of work done in one half cycle of the cylinder oscillation. Here $L/d = 2.0$, $d/D = 0.4$ and $A/D = 0.48$.

energy transferred from the fluid to the cylinder is largely contributed from $\sum W_{fi,1}$. The high-frequency modulation in $W_{fi,2}$ represents the shedding frequency. The work done over a longer time (figure 15*c*) reveals that $\sum W_{fi,2}$, though positive, is also very small, approximately $(1/30)\sum W_{fi,1}$, suggesting a negligibly small contribution to the vibration from the lift associated with higher frequencies.

3.4.2. *Added mass, added damping, and energy transfer model*

The transverse free vibration of a cylinder in a cross-flow may be governed by the following equation (Bearman 1984; Govardhan & Williamson 2000; Williamson & Govardhan 2004)

$$m\ddot{Y} + c\dot{Y} + kY = F_L, \tag{3.1}$$

where m is the total oscillating cylinder mass, c is the structural damping, k is the spring stiffness and F_L is the time-dependent fluid force in the transverse direction (lift force). The overdot represents a derivative with respect to time t. The measured transverse force is often approximated by a sinusoidal function. Thus the motion and force may be given by

$$Y(t) = Y_0 \sin \omega t, \tag{3.2}$$

$$F_L(t) = F_{L0} \sin(\omega t + \phi), \tag{3.3}$$

where Y_0 is the amplitude of the cylinder oscillation, $\omega = 2\pi f$, F_{L0} is the amplitude of the lift force and ϕ is the phase shift between the lift force and cylinder displacement.

The energy W_f transferred from fluid to the cylinder motion for each cycle of oscillation is given by

$$W_f = \int F\,\mathrm{d}Y = \int_t^{t+T} F_{L0}\sin(\omega t' + \phi)\,\mathrm{d}(Y_0 \sin \omega t') = \pi F_{L0} Y_0 \sin\phi. \tag{3.4}$$

Equation (3.4) implies that W_f is directly proportional to F_{L0} and Y_0, and is positive when the lift force leads the displacement by $0° < \phi < 180°$. It should be noted that W_f grows with ϕ when ϕ increases from 0° to 90° and then contracts for further increased ϕ. The energy dissipated by the structural damping is given by

$$W_d = \int (-c\dot{Y})\,\mathrm{d}Y = \int_t^{t+T} -c\omega Y_0 \cos(\omega t')\,\mathrm{d}(Y_0 \sin \omega t') = -\pi c \omega Y_0^2. \tag{3.5}$$

The component of force at the fundamental (body oscillation) frequency is in general considered to be dominant (Alam & Zhou 2007; Assi *et al.* 2010, 2013). This is the most relevant component because the other frequency components do not yield a net contribution to the energy transfer between fluid and structure (Morse & Williamson 2009*a*,*b*). This is also evident in figure 15(*b*–*d*).

The lift force can be split into two, *viz.*

$$F_{L0}\sin(\omega t + \phi) = F_{L0}\cos\phi \sin\omega t + F_{L0}\sin\phi\cos\omega t, \tag{3.6}$$

where the first term on the right-hand side is in phase with the cylinder acceleration. Therefore, (3.1) can be written as

$$\left(m + \frac{F_{L0}\cos\phi}{\omega^2 Y_0}\right)\ddot{Y} + \left(c - \frac{F_{L0}\sin\phi}{\omega Y_0}\right)\dot{Y} + kY = 0. \tag{3.7}$$

Equation (3.7) provides the added mass m_a and added damping c_a, namely,

$$m_a = \frac{F_{L0}\cos\phi}{\omega^2 Y_0} \quad \text{and} \quad c_a = -\frac{F_{L0}\sin\phi}{\omega Y_0}. \tag{3.8a,b}$$

Note that m_a is the effective added mass caused by the lift force in phase with the cylinder acceleration, as opposed to the potential added mass.

Equation (3.7) can now be rewritten as

$$\left(m - \lim_{n\to\infty}\frac{2}{nT(\omega^2 Y_0)^2}\int_t^{t+nT} F\ddot{Y}\,\mathrm{d}t'\right)\ddot{Y} + \left(c - \lim_{n\to\infty}\frac{2}{nT(\omega Y_0)^2}\int_t^{t+nT} F\dot{Y}\,\mathrm{d}t'\right)\dot{Y} + kY = 0. \tag{3.9}$$

The integral terms associated with $\ddot{Y}$ and $\dot{Y}$ in (3.9) provide the means to estimate m_a and c_a, respectively, from experimental data, integrating over an integer number (n) of oscillations. The added mass ratio m_a^* and added damping ratio ζ_a can then be estimated as

$$m_a^* = \frac{m_a}{m_f} = -\frac{8}{nT\rho\pi D^2 l(\omega^2 Y_0)^2}\int_t^{t+nT} F\ddot{Y}\,\mathrm{d}t', \tag{3.10a}$$

$$\zeta_a = \frac{c_a}{c_c} = -\frac{1}{nTm(2\pi f_n)(\omega Y_0)^2}\int_t^{t+nT} F\dot{Y}\,\mathrm{d}t' \quad (\because c_c = 4\pi m f_n), \tag{3.10b}$$

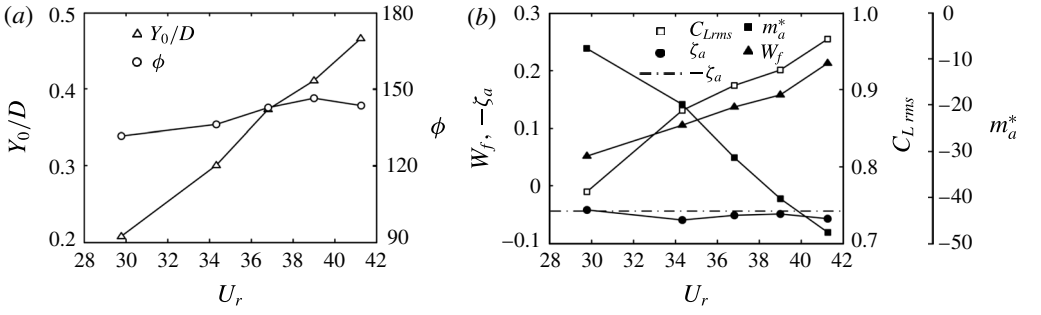

FIGURE 16. Variations in Y_0/D, ϕ, W_f, ζ_a, m_a^* and C_{Lrms} with U_r.

where m_f is the mass of fluid displaced by the cylinder, and c_c is the critical damping. Equations (3.10*a*) and (3.10*b*) provide an averaged m_a^* and an averaged ζ_a over n periods. Having time histories of lift and displacement, we can calculate local m_a^* and ζ_a over one period ($n = 1$) or even instantaneous $m_a^* \propto F\ddot{Y}$ and $\zeta_a \propto F\dot{Y}$.

3.4.3. *Energy transfer during stable vibrations*

At a given U_r, the cylinder vibrates with almost unchanged amplitude ($\pm 4\,\%$). Thus W_f, m_a^* and ζ_a can be calculated from (3.4) and (3.10), where $F_{L0} = \sqrt{2}\,F_{L\,rms}$ and $Y_0 = \sqrt{2}\,Y_{rms}$. The phase lag ϕ is calculated from the cross-correlations $R_{F_{L,Y}}$ between F_L and Y signals obtained simultaneously, *viz.*

$$R_{F_{L,Y}}(\tau) = \frac{\overline{\{Y(t)\}\{F_L(t+\tau)\}}}{[\overline{\{Y(t)\}^2}]^{1/2}[\overline{\{F_L(t+\tau)\}^2}]^{1/2}}, \tag{3.11}$$

where τ is the time delay and t is the time. This equation gives the cross-correlation coefficient as a function of τ. The correlation coefficient is the maximum when the two signals are in phase. Yet, the two signals may not necessarily be in phase. Then a time delay given to one of the signals can make the two signals in phase, producing the maximum correlation coefficient. The time delay corresponding to the maximum correlation is scaled with a phase lag ϕ in angular degrees in one vibration cycle.

Figure 16 shows how C_{Lrms} ($= F_{Lrms}/(0.5\rho U_\infty^2 lD)$), W_f, m_a^*, ζ_a and ϕ vary with U_r or Y_0/D. The structural damping ratio ζ is -0.043. With increasing U_r, Y_0/D rises; so do W_f and C_{Lrms}, with ϕ growing from $\approx 131°$ to $146°$. As noted before, an increase in ϕ beyond $90°$ leads to a drop in W_f. Thus, the rise in Y_0/D is mainly caused by the increased C_{Lrms}, accompanied by an increase in W_f. On the other hand, despite a rise in Y_0/D with U_r, ζ_a changes little, hovering around the structural damping ratio ζ (dashed line). The observation suggests that $|\zeta| = |\zeta_a|$, where ζ and ζ_a are positive and negative, respectively. The small departure in the magnitude of ζ_a from ζ may originate from the assumption of sinusoidal Y and F_L variations (3.8). For a stable vibration, the energy transferred from fluid to structure should be equal to the energy dissipated by structural damping; that is, $W_f + W_d = 0$ (equations (3.4) and (3.5)), i.e. $\pi F_{L0} Y_0 \sin\phi - \pi c\omega Y_0^2 = 0$. Then, in view of (3.8), we obtain

$$c = \frac{F_{L0}\sin\phi}{\omega Y_0} = -c_a \quad \text{or} \quad c + c_a = 0. \tag{3.12a,b}$$

In other words, the added damping, invariant with U_r, for a stable vibration simply compensates the structural damping so that the net damping is zero. Note that the energy dissipation due to the structural damping is proportional to Y_0^2 based on (3.5). The increase in Y_0/D with U_r thus requires more work done by the lift force. The $C_{L\,rms}$ is thus augmented accordingly to compensate the dissipation. Furthermore, as ϕ moves further away from 90° with increasing U_r, additional increase in $C_{L\,rms}$ is required to compensate its associated decrease in W_f. The relationship between Y_0, F_{L0} and ϕ, which may cast light upon the above observation, can be obtained by equating (3.4) and (3.5), *viz.* $W_f + W_d = 0$. Then

$$Y_0 = \frac{F_{L0}\sin\phi}{c\omega}. \tag{3.13}$$

That is, Y_0 is directly proportional to F_{L0}.

Finally, the relationship between m_a^* and U_r may be analysed. Interestingly, m_a^* decreases monotonically from approximately -8 to -47 as U_r varies from 29.8 to 41.4 (figure 16*b*).

3.5. *Vibration generation mechanism*

Previous data analysis casts light upon the flow physics behind the stable cylinder vibration. The questions we must ask first and foremost are how the vibration is initiated and what is the most important factor or parameter involved in this initiation process, which are crucial for finding means to control the vibration. This requires a thorough understanding of what happens in the process when the cylinder vibration starts and grows in amplitude.

Two scenarios are considered to address the issues raised. (I) The wind tunnel is not operated and there is no flow. Set the tunnel fan frequency at 13.8 Hz via the frequency inverter, at which U_r is 41.4 ($A/D = 0.48$) given a steady flow, and the measurement instruments are ready for data acquisition. Then switch on the tunnel and let the wind speed increase continuously from $U_r = 0$ to 41.4. The cylinder starts to vibrate at an intermediate U_r, and the vibration amplitude grows till it reaches a constant value. Our focus is given to the transitional stage where the cylinder vibration starts and grows in amplitude. (II) The tunnel is under steady operation and the corresponding U_r is 41.4. The cylinder is held fixed by two air-compressor-operated clamps installed separately at its two ends (figure 17). One single switch is used to control both clamps so that the release of the clamping force takes place simultaneously at both ends of the cylinder. Once released, the cylinder starts to vibrate from its stationary state to the stable vibration. In order to capture the entire transition process, the data acquisition starts a few seconds before the release of the clamping force.

3.5.1. *Force and vibration characteristics in the initiation stage*

The measured signals of U_r, Y/D, filtered C_L (low-pass-filtered at a cut-off frequency of 20 Hz) are presented for the two cases in figure 18. In case I, U_r rises continuously from 8.5 at $t = 0$ s (arbitrary) to 41.4 at $t = 16.8$ s and then remains unchanged (figure 18*a*). The Y/D remains at 0 until $t = 8$ s when $U_r = 28.3$, and then starts to grow (figure 18*c*). At $t \approx 9$ s, Y/D undergoes a rapid increase, reaching approximately 0.48 at $t = 12$ s, and then remains unchanged. It should be pointed out that, while U_r changes from approximately 37 at $t = 12$ s to 41.4 at $t = 16.8$ s, Y/D remains nearly constant, that is, Y/D becomes saturated earlier than

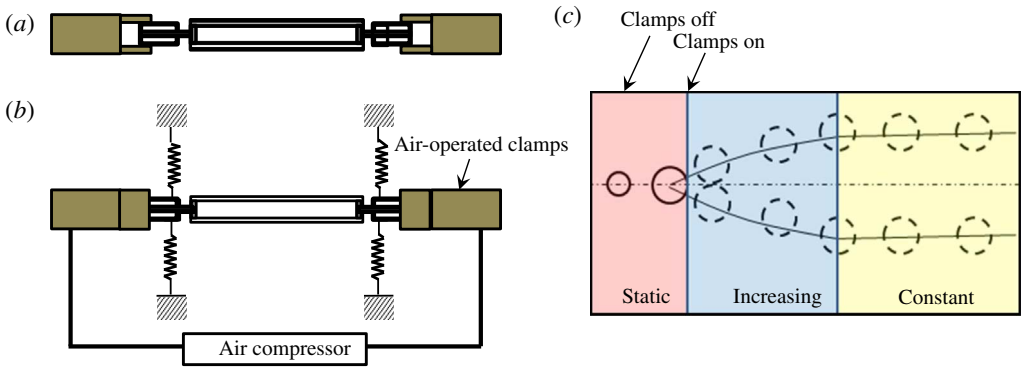

FIGURE 17. (Colour online) Air-operated two-finger clamp (hand) to hold and release the cylinder: (*a*) top view, (*b*) side view. (*c*) A sketch of the transition process of amplitude growth.

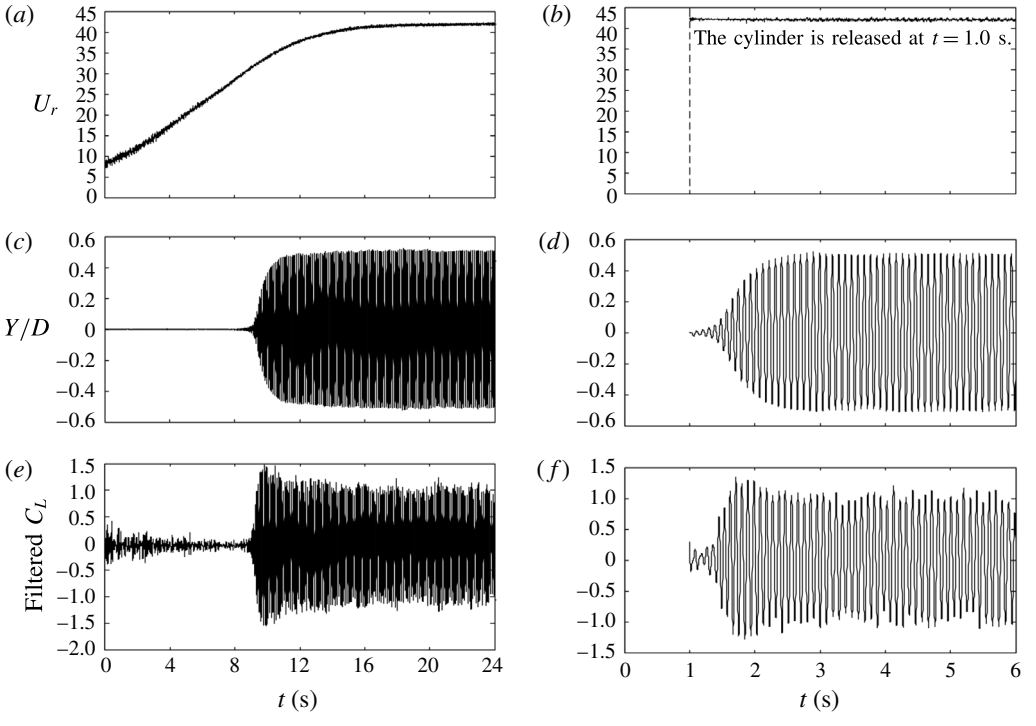

FIGURE 18. Time histories of U_r, Y/D and 20 Hz low-pass-filtered C_L for (*a*,*c*,*e*) case I and (*b*,*d*,*f*) case II.

U_r. As shown in figure 18(*e*), the C_L amplitude grows very rapidly from 0.10 (the corresponding $A/D = 0.02$) at $t = 9$ s to 1.48 ($A/D = 0.32$) at 9.8 s. After $t = 9.8$ s, the C_L amplitude retreats slowly up to $t = 13$ s and then remains more or less constant. In case II, the cylinder is initially fixed with $U_r = 41.4$ and then suddenly released at $t = 1$ s (figure 18*b*). The Y/D amplitude increases from approximately 0 to 0.48 at $t = 1$–2.9 s, and then remains constant (figure 18*d*). The C_L grows rapidly

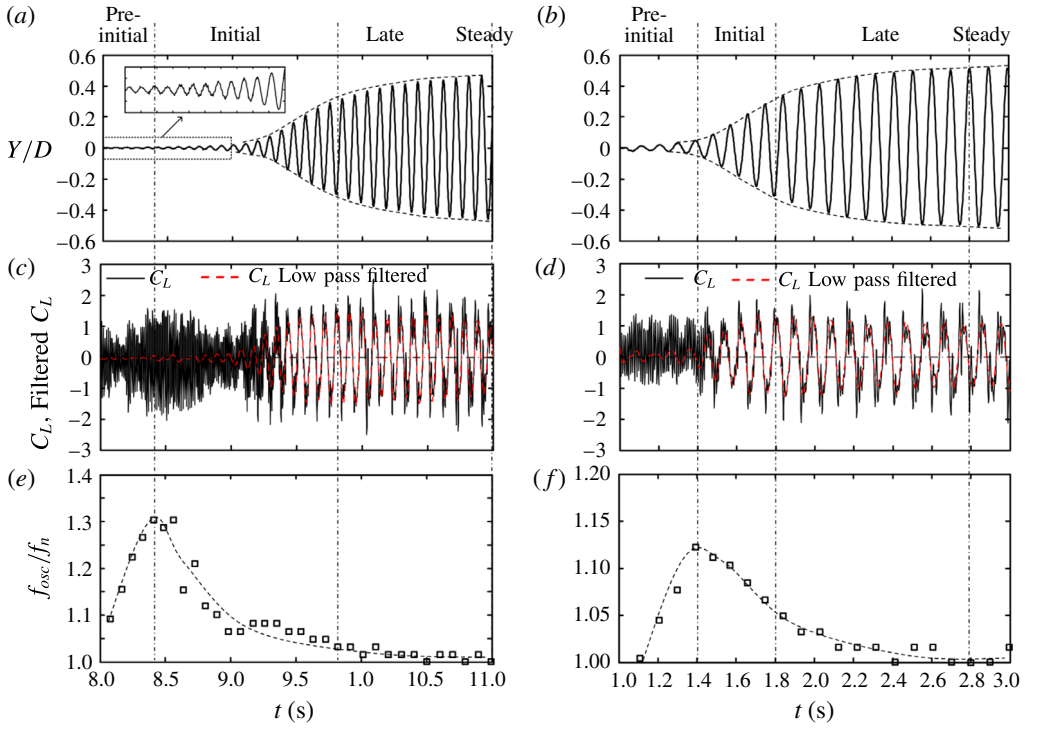

FIGURE 19. (Colour online) Time histories of Y/D, C_L and f_{osc}/f_n in the transition process for (*a*,*c*,*e*) case I and (*b*,*d*,*f*) case II. The dashed lines in (*a*) and (*b*) enclose the Y/D amplitude and those in (*e*) and (*f*) denote the trend of f_{osc}/f_n. The dashed red lines in (*c*) and (*d*) are 20 Hz low-pass-filtered C_L.

in amplitude up to $t = 1.8$ s, followed by a small contraction before reaching a rather stable state for $t > 2.5$ s (figure 18*f*). In both cases, an interesting observation is that C_L reaches its maximum magnitude in the transitional process before Y/D reaches its stable amplitude. As such, we divide the transitional process into two: the initial transition where both Y/D and C_L grow in amplitude, and the late transition where Y/D grows but C_L slowly decreases in amplitude. The division point between the two transitions is characterized by the maximum amplitude of C_L. The underlying physics behind the two transitions is different and will be discussed later. A close examination of the variation in Y/D unveils that Y/D grows rapidly in amplitude in the initial transition and mildly in the late transition, characterized by positive and negative curvatures, respectively. The maximum amplitude of C_L occurs at the inflection point where the curvature is zero.

We next explore how the vibration is generated or how the vibration amplitude grows based on the signals of Y/D, C_L, low-pass-filtered C_L at a cut-off frequency of 20 Hz and f_{osc}/f_n in the transition stage of $t = 8$–11 s for case I and $t = 1$–3 s for case II (figure 19). The f_{osc}/f_n in each cycle is simply estimated from the cylinder displacement of one peak to the next, i.e. one oscillation period (T) and $f_{osc} = 1/T$. The sampling frequency of the Y/D signal is 654 Hz, corresponding to an uncertainty in f_{osc} of $\pm 0.0156 f_n$. The Y/D signal is first 20 Hz low-pass-filtered before estimating T so that the peaks may be identified with reasonable accuracy. In case I, Y/D over $t = 8$–8.4 s experiences largely a sinusoidal variation with some minor high-frequency

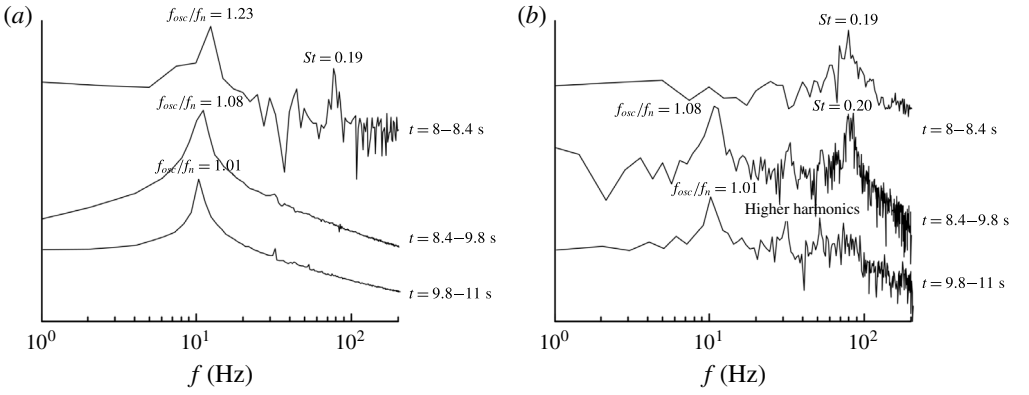

FIGURE 20. Power spectral density functions (*a*) E_Y of Y and (*b*) E_{CL} of C_L over different durations of time during the transition process for case I.

fluctuations due to the natural vortex shedding (refer to the inset of figure 19*a*). However, C_L fluctuates largely at the natural shedding frequency, which is much higher than the predominant frequency in Y/D. The C_L fluctuation at the cylinder oscillation frequency or the filtered C_L (figure 19*c*) is negligibly small at $t < 8.4$ s and starts to grow at $t \approx 8.4$ s where the C_L fluctuation at the shedding frequency is largest. At $t > 8.4$ s, the C_L fluctuation decays at the shedding frequency but grows at the oscillation frequency. The observation is interesting, suggesting that the vibration may be initiated by natural vortex shedding. At $t = 9.0$–9.4 s where Y/D grows rapidly in amplitude, the high-frequency fluctuation in C_L still exists, along with the low-frequency fluctuation. At $t > 9.4$ s where Y/D continues to grow in amplitude, the low-frequency fluctuation in C_L becomes dominant, overwhelming the high-frequency fluctuation. As discussed before, the C_L amplitude associated with the cylinder vibration frequency grows up to $t \approx 9.8$ s and then dwindles, its maximum occurring at $t \approx 9.8$ s. The Y/D increases rapidly in amplitude over $t = 8.4$–9.8 s with a positive curvature (amplitude traced by the dashed line) and weakly with a negative curvature. Note that the curvature discussed here is based on the upper dashed line. Therefore, the durations of $t = 8.4$–9.8 s and $t > 9.8$ s are referred to as the initial and late transitions, respectively.

It is interesting to find out whether the cylinder oscillation frequency varies in the transition stage. As shown in figure 19(*e*), f_{osc}/f_n jumps from 1.09 to approximately 1.3 at $t = 8.4$ s where the vibration is initiated, then declines up to $t = 9.8$ s. At $t > 9.8$ s, f_{osc}/f_n varies little, slightly larger than 1. The duration of $t = 8.0$–8.4 s where f_{osc}/f_n rises quickly is referred to as the pre-initial transition. Figure 20 presents the power spectra of Y/D and C_L over $t = 8$–8.4 s, 8.4–9.8 s and 9.8–11 s, corresponding to the pre-initial, initial and late transitions, respectively. The Y/D spectrum over $t = 8$–8.4 s (figure 20*a*) displays two pronounced peaks, corresponding to the cylinder oscillation and shedding frequencies, respectively. The magnitude of f_{osc}/f_n is approximately 1.23. The C_L spectrum over the same duration shows only one pronounced peak at the shedding frequency (figure 20*b*). In the initial transition ($t = 8.4$–9.8 s), the Y/D spectrum exhibits only one large peak at the cylinder oscillation frequency but the C_L spectrum shows peaks at both cylinder oscillation and shedding frequencies, the peak at the oscillation frequency being smaller in amplitude than that at $t = 8$–8.4 s ($f_{osc}/f_n = 1.08$). On the other hand, in the late

transition ($t = 9.8$–11 s), the Y/D spectrum indicates that the cylinder oscillates at $f_{osc}/f_n \approx 1$ and the C_L spectrum shows a tiny peak at the shedding frequency (figure 20*a*,*b*). In summary, f_{osc}/f_n increases in the pre-initial transition and reaches the maximum at the end of the pre-initial transition. The f_{osc}/f_n value decreases in the initial transition and becomes almost constant in the late transition and afterwards. In the free vibration of a single cylinder, f_{osc} in the lock-in range varies with U_r at small $m^*\zeta$ (< 0.05) and low m^* (< 10), and may deviate greatly from f_n (Khalak & Williamson 1999), while $f_{osc}/f_n \approx 1$ at large mass ratios, i.e. $m^* > 100$ (Govardhan & Williamson 2000). Govardhan & Williamson (2000) identified the initial, upper and lower branches in the VE regime for a single cylinder at small $m^*\zeta$ ($= 0.0013$), and then obtained an expression for the vibration frequency in the lower branch, which takes into account the added mass ratio m_a^* and is valid in the case of low $m^*\zeta$. Mittal & Kumar (2001) also noted the departure between f_{osc} and f_n for two tandem cylinders in cross-flow with $m^* = 1.5$ and $m^*\zeta = 0.00051$. However, the present large m^* ($= 275$) and $m^*\zeta$ ($= 0.58$) result in $f_{osc}/f_n \approx 1$ in a steady-state vibration (figure 19) for all U_r examined. Therefore, the dependence of f_{osc}/f_n on U_r is not presented.

The same observation is made for case II, where the pre-initial, initial and late transitions correspond to $t = 1$–1.4 s, $t = 1.4$–1.8 s and $t > 1.8$ s, respectively. It may be concluded that natural vortex shedding is a predominant excitation source of the cylinder vibration in the pre-initial transition and initiates the vibration. However, both vortex shedding and fluctuating lift at f_{osc}/f_n make important contributions to the cylinder vibration in the initial transition; yet it is the latter that is largely responsible for the vibration in the late transition. In the previous section, it has been demonstrated that in the stable vibration the gap shear layers interact vigorously with the vibrating downstream cylinder. It is now clear that in the transitional process the pre-initial transition is characterized by an interaction between natural vortex shedding and the cylinder; the gap shear layer joins the interaction between natural vortex shedding in the initial transition. However, the late transition is dominated by the interaction between the gap shear layer and the cylinder, which persists in the stable vibration.

3.5.2. *Energy transfer and added mass*

The roles of ϕ, W_f and m_a^* in the transition need to be clarified. The amplitude of the filtered C_L is rather irregular and less sinusoidal in the first half ($t = 8.4$–9.0 s) of the initial transition (figure 19*c*) but becomes sinusoidal in the second half ($t > 9.0$ s). Similarly, in case II, the filtered C_L is sinusoidal at $t > 1.4$ s when the initial transition starts. In the following discussion, the starting time is made at $t = 9.0$ s for case I and $t = 1.4$ s for case II. Figure 21 shows the signals of Y_0/D, C_{L0}, ϕ and f_{osc}/f_n for the two cases, where C_{L0} is the amplitude of the filtered C_L in each cycle. In case I, C_{L0} grows rapidly in the initial transition and approaches its maximum at $t = 9.8$ s at which $Y_0/D = 0.32$. In the same duration, ϕ increases from approximately 90° to 134° but f_{osc}/f_n decreases monotonically from 1.09 to 1.01, both maintaining essentially a constant value at $t > 11$ s (figure 21*c*,*e*). The changes in ϕ and f_{osc}/f_n in the initial transition are largely connected to the gradual replacement of natural vortex shedding by the gap shear layers in the interaction with the downstream cylinder. In the late transition ($t = 9.8$–11 s), C_{L0} retreats to approximately 1.1 with small variations in ϕ and f_{osc}/f_n, whilst Y_0/D is augmented to 0.48. A similar observation is made for case II (figure 21*b*,*d*,*f*).

The values of W_f, W_d and W_t ($= W_f + W_d$) vary at different instants and are calculated over one period for cases I and II (figure 22*a*,*b*). The W_f and W_d values

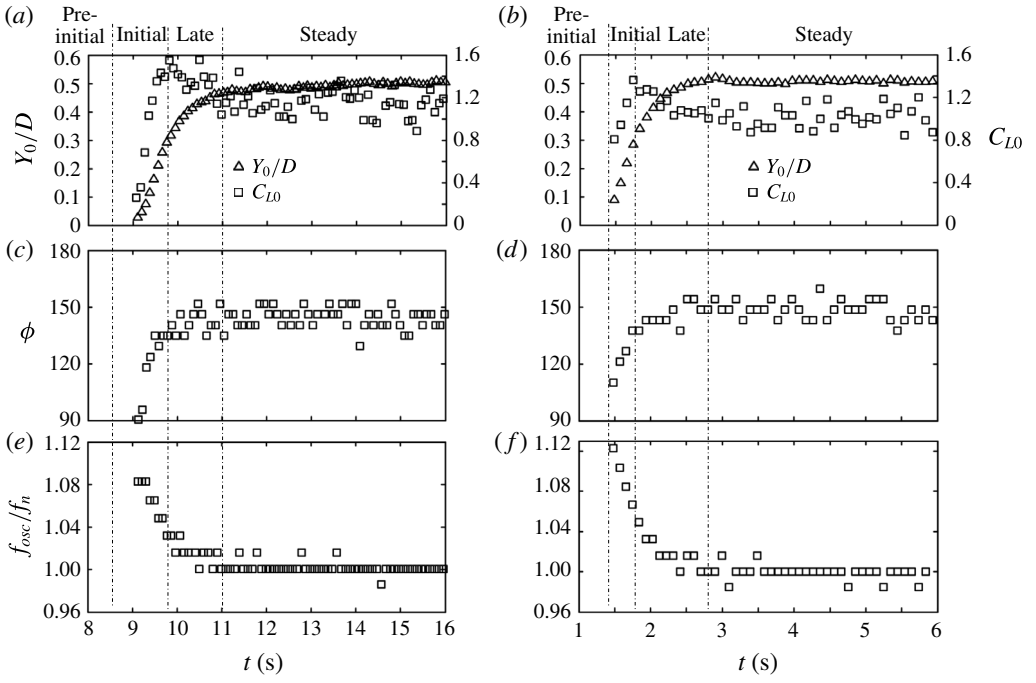

FIGURE 21. Time histories of Y_0/D, C_{L0}, ϕ and f_{osc}/f_n for (a,c,e) case I and (b,d,f) case II.

rise and decline, respectively, in the initial and late transitions and show no change after the late transition. On the other hand, W_t grows rapidly in the initial transition, reaching a maximum before declining in the late transition. A value $W_t > 0$ means $W_f > W_d$, i.e. the energy transferred from the fluid to the cylinder is larger than the energy dissipated through structural damping. Therefore, $W_t > 0$ implies that there is an excess of energy used to enlarge Y_0/D. Naturally, the growth in W_t in the initial transition is accompanied by a rise in Y_0/D. In the late transition, the slowdown in the Y_0/D growth is associated with a decline in W_t. Once $W_t \approx 0$, Y_0/D becomes constant. Both W_f and W_d depend on Y_0/D, as is evident in figure 22(c,d), where $-W_d$ is shown to make clear the difference between W_f and W_d. The difference between W_f and W_d grows from $Y_0/D = 0$ to 0.32 and then tapers off, essentially collapsing together at $Y_0/D \approx 0.48$.

Finally, let us turn our attention to m_a^* and ζ_a. In case I, the vortex shedding frequency was detected in both Y/D and C_L in the pre-initial transition over t = 8–8.4 s (figure 20). Then, m_a^* and ζ_a are calculated based on the shedding frequency in the pre-initial transition but on the structural vibration for the rest of the transition. Interestingly, both m_a^* and ζ_a (figure 23) are initially positive at $t = 8$ s and then drop rapidly in the pre-initial transition. It seems plausible that the vibration is initiated by negative m_a^* and ζ_a, i.e. vortex shedding contributes to the initiation of the structural vibration. At $t = 8.4$ s–9.0 s, both m_a^* and ζ_a cannot be determined as discussed in § 3.5.1. At $t > 9.0$ s, both m_a^* and ζ_a are highly negative, showing a rapid rise from -105 to -58 and from -0.26 to -0.07, respectively, in the initial transition and then a mild growth in the late transition. Their values go up in the stable vibration state to $m_a^* \approx -47$ and $\zeta_a \approx -0.043$, which is equal in magnitude to

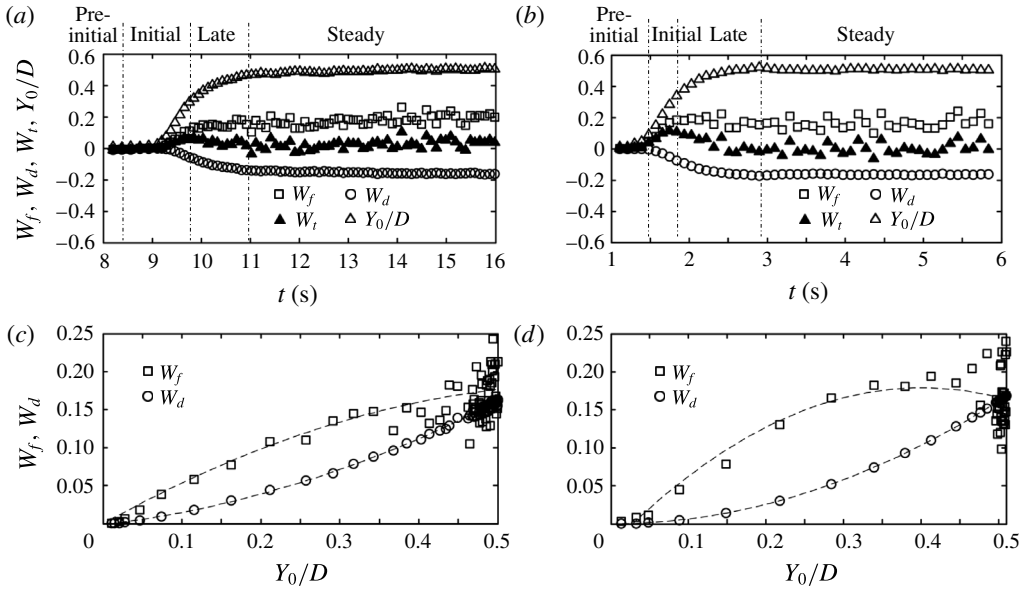

FIGURE 22. Time histories of W_f, W_d, W_t and Y_0/D in each period during the transition for (*a*) case I and (*b*) case II. Variations in W_f and W_d with increase in Y_0/D for (*c*) case I and (*d*) case II. Dashed lines are the least-squares curve fit to a second-order polynomial.

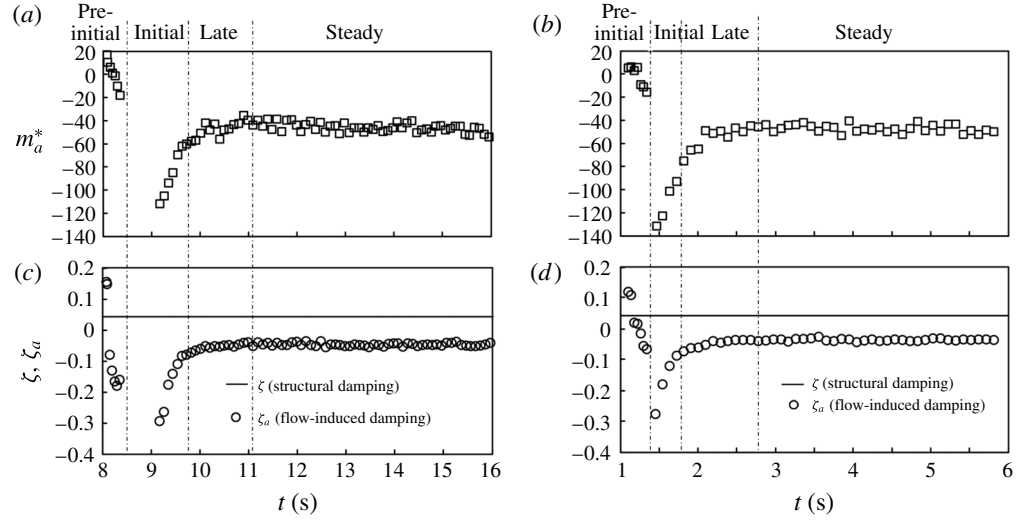

FIGURE 23. Time histories of m_a^* and ζ_a for (*a*,*c*) case I and (*b*,*d*) case II.

the structural damping, i.e. $\zeta_a + \zeta = 0$ (figure 23*c*). A similar observation is made in case II (figure 23*b*,*d*). It may be concluded that, during the growth of vibration, an effective damping ratio of the fluid–cylinder system is negative, i.e. $\zeta + \zeta_a < 0$, resulting in an exponential growth in the vibration amplitude, while this effective damping ratio is zero, i.e. $\zeta + \zeta_a = 0$, at the stable vibration state.

Following (3.4) and (3.5), a stable vibration for $c = 0$ (undamped) leads to $\phi = 0°$ or 180° and hence $c_a = 0$ (3.8). As such, for an undamped cylinder, ϕ is found to be 0° for the initial branch (Govardhan & Williamson 2000; Prasanth & Mittal 2008) and 180° for the upper and lower branches in the lock-in regime; ϕ is discontinuous between the initial and upper branches (Prasanth & Mittal 2008). For these values of ϕ, (3.4) yields $W_f = 0$, which is consistent with our intuition.

4. Conclusions

A systematic experimental investigation is performed on the flow-induced vibration of a cylinder in the wake of an upstream stationary cylinder of different diameters. The parameters examined include d/D (= 0.2–1.0), L/d (= 1.0–5.5) and U_r (= 3.8–44). The investigation covers three aspects, i.e. the dependence of violent structural vibration on d/D and L/d, the flow physics or mechanisms behind the violent vibration, and the initiation of the vibration, leading to the following conclusions.

Six flow regimes are identified, and their dependences on d/D and L/d are given in figure 5. Regime I corresponds to the occurrence of a violent vibration on the downstream cylinder, which is the focus of this study. There is little or no vibration in the other regimes, which are distinguished based on the relationship between the frequencies f_{v1} and f_{v2} of vortex shedding from the upstream and downstream cylinders, respectively. In regime II, flow reattachment occurs, and $f_{v2} = f_{v1}$. A pronounced peak also occurs at $2f_{v2}$ in E_{u2}. The flow is bistable in regime III, where f_{v2} may or may not be the same as f_{v1}, depending on d/D. The other three regimes are all characterized by vortex co-shedding from the two cylinders, though $f_{v2} = f_{v1}$ in regime IV, $f_{v2} = f_{v1}$ but a pronounced peak occurs at $0.5f_{v2}$ in E_{u2} in regime V, and $f_{v2} \neq f_{v1}$ in regime VI.

The dependence of the violent cylinder vibration on d/D and L/d in regime I is characterized by an increase in L/d leading to a decrease in d/D and also a reduced range of d/D (figure 5). At a small d/D, the upstream cylinder wake is narrow and the shear layer is prone to switching its direction from one side to the other, thus exciting the downstream cylinder and causing a violent vibration. The downstream cylinder may be excited at a small incident angle, associated with small d/D, given a large L/d. The violent cylinder vibration is primarily connected to the lift force induced by the switching gap shear layers from one side to the other of the downstream cylinder, as is evidenced by the synchronization of the switching frequency and the cylinder oscillation frequency. A hysteresis phenomenon has been found during the cycle of the cylinder vibration; the phase-averaged vorticity contours and pressure distribution around the cylinder from $Y/D = 0$ to Y_0/D (figure 9*a–c*, figure 13*a–c*) display considerable differences from their counterparts from $Y/D = Y_0/D$ to 0 (figure 9*c–e*, figure 13*c–e*). The result implies a phase lag between C_L and Y/D. This phase lag is physically connected to the nonlinear flow-induced damping.

When the cylinder vibrates violently, two predominant frequencies are identified in the spectra of u_2 captured behind the cylinders, which are associated with natural vortex shedding and the cylinder vibration at f_{osc}, respectively. Two types of vortices are generated during the cylinder vibration. The first type is induced by the gap shear layers impinging on the downstream cylinder; the vortices occur in general about the centreline and decay rapidly. The second originates from the shear layer separation when the downstream cylinder is at its maximum displacement; being far away from the centreline, the vortices persist downstream and dominate the wake. When the first

type of vortex is generated, the work done is positive, that is, the cylinder absorbs energy from the flow, resulting in a sustainable vibration. On the other hand, the work done is negative during the generation of the second type, which acts to weaken the vibration.

How the structural vibration is initiated is unveiled. Two scenarios are examined. Firstly, the flow is increased continuously from $U_r = 0$ to a value corresponding to a violent vibration and the cylinder is allowed to vibrate freely. Secondly, given a flow that is adequate to produce a large-amplitude vibration, the cylinder is fixed initially at both ends and then suddenly released for transverse free vibration, from $Y_0/D = 0$ to its stable vibration. In both cases, Y_0/D grows from zero to its stable value. The transition or growth process is characterized by three stages. In the pre-initial stage, Y_0/D is very small and C_L is dominated by the fluctuation at the vortex shedding frequency. Meanwhile, the added damping and added mass decline and hence f_{osc}/f_n grows gradually. The corresponding W_t is small. In the initial transition stage, Y_0/D grows rapidly, accompanied by an exponential rise in both C_L and ϕ. Meanwhile, f_{osc}/f_n drops since both added damping and added mass go up. Thus, W_t increases rapidly, reaching its maximum at the end of this stage. In the late transition stage, the growth in Y_0/D slows down and C_L decreases, while both ζ_a and m_a^* keep rising, albeit very slowly, resulting in a reduced f_{osc}/f_n. The slowdown in the growing Y_0/D is associated with a drop in W_t, which is almost zero as Y_0/D approaches a constant value. It has been found that natural vortex shedding initiates the cylinder vibration in the pre-initial transition, though both vortex shedding and the gap shear layer switching are responsible for a rapid growth in vibration in the initial transition. Yet, it is the gap shear layer switching that accounts for the sustainable violent vibration in the late transition.

Acknowledgements

M.M.A. wishes to acknowledge the support given to the authors by the National Natural Science Foundation of China through grant 11672096 and by the Research Grant Council of Shenzhen Government through grant JCYJ20160531191442288.

Nomenclature

A	root-mean-square (r.m.s.) value of vibration response multiplied by $\sqrt{2}$
ζ	structural damping
ζ_a	added damping
C_L	lift force coefficient
C_{L0}	the amplitude of lift force coefficient
$C_{L\,rms}$	fluctuating (r.m.s.) lift coefficient
C_P	pressure coefficient
d	upstream cylinder diameter
D	downstream cylinder diameter
f	frequency
f_n	natural frequency of the cylinder system
f_{osc}	cylinder oscillation frequency
f_v	vortex shedding frequency
f_{v1}	vortex shedding frequency in the gap of the cylinders

$f_{v2}(f'_{v2})$	vortex shedding frequency behind the cylinders
F	fluid force in the transverse direction
F_{L0}	amplitude of fluid force
k	spring stiffness
l	length of the cylinder
L	spacing between the centre of the upstream cylinder to the forward stagnation point of the downstream cylinder
m	cylinder mass
m_a	added mass
m_a^*	added mass ratio
m^*	mass ratio $(= 4m/(\pi\rho D^2 l))$
St	Strouhal number
U_∞	free-stream velocity
U_r	reduced velocity $(= U_\infty/f_n D)$
VE	vortex excitation
W_f	energy transferred from the fluid to the cylinder motion, over one cycle of oscillation
W_d	energy dissipated by the structural damping over one cycle of oscillation
W_t	total energy transfer $(= W_f + W_d)$
Y	cylinder displacement
Y_0	maximum amplitude of oscillation
ω	angular frequency $(= 2\pi f_{osc})$
ρ	density of fluid
δ	logarithmic decrement of amplitudes
ϕ	phase lag between fluid force and cylinder displacement
(x, y, z)	coordinate with the origin at the downstream cylinder centre
(x', y', z')	coordinate with the origin at the upstream cylinder centre

REFERENCES

ALAM, M. M. 2014 The aerodynamics of a cylinder submerged in the wake of another. *J. Fluids Struct.* **51**, 393–400.

ALAM, M. M. 2016 Lift forces induced by the phase lag between the vortex sheddings from two tandem bluff bodies. *J. Fluids Struct.* **65**, 217–237.

ALAM, M. M. & MEYER, J. P. 2013 Global aerodynamic instability of twin cylinders in cross flow. *J. Fluids Struct.* **41**, 135–145.

ALAM, M. M., MORIYA, M., TAKAI, K. & SAKAMOTO, H. 2003 Fluctuating fluid forces acting on two circular cylinders in a tandem arrangement at a subcritical Reynolds number. *J. Wind Engng Ind. Aerodyn.* **91**, 139–154.

ALAM, M. M. & SAKAMOTO, H. 2005 Investigation of Strouhal frequencies of two staggered bluff bodies and detection of multistable flow by wavelets. *J. Fluids Struct.* **20**, 425–449.

ALAM, M. M. & ZHOU, Y. 2007 The turbulent wake of an inclined cylinder with water running. *J. Fluid Mech.* **589**, 261–303.

ALAM, M. M. & ZHOU, Y. 2008 Strouhal numbers, forces and flow structures around two tandem cylinders of different diameters. *J. Fluids Struct.* **24**, 505–526.

ARIE, M., KIYA, M., MORIYA, M. & MORI, H. 1983 Pressure fluctuations on the surface of two circular cylinders in tandem arrangement. *Trans. ASME J. Fluids Engng* **105** (2), 161–166.

ASSI, G. R. 2014 Wake-induced vibration of tandem cylinders of different diameters. *J. Fluids Struct.* **50**, 329–339.

ASSI, G. R. S., BEARMAN, P. W., CARMO, B. S., MENEGHINI, J. R., SHERWIN, S. J. & WILLDEN, R. H. J. 2013 The role of wake stiffness on the wake-induced vibration of the downstream cylinder of a tandem pair. *J. Fluid Mech.* **718**, 210–245.

ASSI, G. R. S., BEARMAN, P. W. & MENEGHINI, J. R. 2010 On the wake-induced vibration of tandem circular cylinders: the vortex interaction excitation mechanism. *J. Fluid Mech.* **661**, 365–401.

BEARMAN, P. W. 1984 Vortex shedding from oscillating bluff bodies. *Annu. Rev. Fluid Mech.* **16** (1), 195–222.

BEARMAN, P. W., GARTSHORE, I. S., MAULL, D. J. & PARKINSON, G. V. 1987 Experiments on flow-induced vibration of a square-section cylinder. *J. Fluids Struct.* **1** (1), 19–34.

BOKAIAN, A. & GEOOLA, F. 1984*a* Wake-induced galloping of two interfering circular cylinders. *J. Fluid Mech.* **146**, 383–415.

BOKAIAN, A. & GEOOLA, F. 1984*b* Proximity-induced galloping of two interfering circular cylinders. *J. Fluid Mech.* **146**, 417–449.

BRIKA, D. & LANEVILLE, A. 1997 Wake interference between two circular cylinders. *J. Wind Engng Ind. Aerodyn.* **72**, 61–70.

BRIKA, D. & LANEVILLE, A. 1999 The flow interaction between a stationary cylinder and a downstream flexible cylinder. *J. Fluids Struct.* **13**, 579–606.

CARMO, B. S., MENEGHINI, J. R. & SHERWIN, S. J. 2010 Possible states in the flow around two circular cylinders in tandem with separations in the vicinity of the drag inversion spacing. *Phys. Fluids* **22** (5), 054101.

COOPER, K. R. & WARDLAW, R. L. 1971 Aeroelastic instabilities in wakes. In *Proc. 3rd Int. Conf. on Wind Effects on Buildings and Structures*, pp. 647–655. Tokyo.

DIELEN, B. & RUSCHEWEYH, H. 1995 Mechanism of interference galloping of two identical circular cylinders in cross flow. *J. Wind Engng Ind. Aerodyn.* **54**, 289–300.

GERRARD, J. H. 1966 The mechanics of the formation region of vortices behind bluff bodies. *J. Fluid Mech.* **25** (02), 401–413.

GOVARDHAN, R. & WILLIAMSON, C. H. K. 2000 Modes of vortex formation and frequency response of a freely vibrating cylinder. *J. Fluid Mech.* **420**, 85–130.

HORI, E. I. 1959 Experiments on flow around a pair of parallel circular cylinders. In *Proc. 9th Japan Nut. Cong. Appl. Mech.*, pp. 231–234. Tokyo.

HOVER, F. S. & TRIANTAFYLLOU, M. S. 2001 Galloping response of a cylinder with upstream wake interference. *J. Fluids Struct.* **15**, 503–512.

HUANG, S. & SWORN, A. 2011 Some observations of two interfering VIV circular cylinders of unequal diameters in tandem. *J. Hydrodyn. Ser.* B **23** (5), 535–543.

HUANG, S. & SWORN, A. 2013 Interference between two stationary or elastically supported rigid circular cylinders of unequal diameters in tandem and staggered arrangements. *J. Offshore Mech. Arctic Engng* **135** (2), 021803.

IGARASHI, T. 1981 Characteristics of the flow around two circular cylinders arranged in tandem: 1st report. *Bull. JSME* **24** (188), 323–331.

IGARASHI, T. 1982 Characteristics of a flow around two circular cylinders of different diameters arranged in tandem. *Bull. JSME* **25**, 349–357.

IGARASHI, T. 1984 Characteristics of the flow around two circular cylinders arranged in tandem: 2nd report. Unique phenomenon at small spacing. *Bull. JSME* **27** (233), 2380–2387.

JEON, D. & GHARIB, M. 2004 On the relationship between the vortex formation process and cylinder wake vortex patterns. *J. Fluid Mech.* **519**, 161–181.

JESTER, W. & KALLINDERIS, Y. 2003 Numerical study of incompressible flow about fixed cylinder pairs. *J. Fluids Struct.* **17**, 561–577.

KHALAK, A. & WILLIAMSON, C. H. 1997 Investigation of relative effects of mass and damping in vortex-induced vibration of a circular cylinder. *J. Wind Engng Ind. Aerodyn.* **69**, 341–350.

KHALAK, A. & WILLIAMSON, C. H. K. 1999 Motions, forces and mode transitions in vortex-induced vibrations at low mass-damping. *J. Fluids Struct.* **13** (7–8), 813–851.

KIM, S., ALAM, M. M., SAKAMOTO, H. & ZHOU, Y. 2009 Flow-induced vibrations of two circular cylinders in tandem arrangement. Part 1: Characteristics of vibration. *J. Wind Engng Ind. Aerodyn.* **97**, 304–311.

KNISELY, C. W. & KAWAGOE, M. 1990 Force–displacement measurements on closely spaced tandem cylinders. *J. Wind Engng Ind. Aerodyn.* **33** (1–2), 81–90.

LAM, K. M. & TO, A. P. 2003 Interference effect of an upstream larger cylinder on the lock-in vibration of a flexibly mounted circular cylinder. *J. Fluids Struct.* **17**, 1059–1078.

LANEVILLE, A. & BRIKA, D. 1999 The fluid and mechanical coupling between two circular cylinders in tandem arrangement. *J. Fluids Struct.* **13**, 967–986.

LEONTINI, J. S., STEWART, B. E., THOMPSON, M. C. & HOURIGAN, K. 2006 Predicting vortex-induced vibration from driven oscillation results. *Appl. Math. Model.* **30** (10), 1096–1102.

LIN, C. & HSIEH, S. C. 2003 Convection velocity of vortex structures in the near wake of a circular cylinder. *J. Engng Mech.* **129** (10), 1108–1118.

LIN, J. C., YANG, Y. & ROCKWELL, D. 2002 Flow past two cylinders in tandem: instantaneous and averaged flow structure. *J. Fluids Struct.* **16** (8), 1059–1071.

LJUNGKRONA, L., NORBERG, C. H. & SUNDEN, B. 1991 Free-stream turbulence and tube spacing effects on surface pressure fluctuations for two tubes in an in-line arrangement. *J. Fluids Struct.* **5** (6), 701–727.

MAHIR, N. & ROCKWELL, D. 1996 Vortex formation from a forced system of two cylinders. Part I: tandem arrangement. *J. Fluids Struct.* **10**, 473–490.

MITTAL, S. & KUMAR, V. 2001 Flow-induced oscillations of two cylinders in tandem and staggered arrangements. *J. Fluids Struct.* **15** (5), 717–736.

MORSE, T. L. & WILLIAMSON, C. H. K. 2009*a* Prediction of vortex-induced vibration response by employing controlled motion. *J. Fluid Mech.* **634**, 5–39.

MORSE, T. L. & WILLIAMSON, C. H. K. 2009*b* Fluid forcing, wake modes, and transitions for a cylinder undergoing controlled oscillations. *J. Fluids Struct.* **25**, 697–712.

PAN, Z. Y., CUI, W. C. & MIAO, Q. M. 2007 Numerical simulation of vortex-induced vibration of a circular cylinder at low mass-damping using RANS code. *J. Fluids Struct.* **23** (1), 23–37.

PRASANTH, T. K. & MITTAL, S. 2008 Vortex-induced vibrations of a circular cylinder at low Reynolds numbers. *J. Fluid Mech.* **594**, 463–491.

RAHMANIAN, M., ZHAO, M., CHENG, L. & ZHOU, T. 2012 Two-degree-of-freedom vortex-induced vibration of two mechanically coupled cylinders of different diameters in steady current. *J. Fluids Struct.* **35**, 133–159.

RUSCHEWEYH, H. & DIELEN, B. 1992 Interference galloping-investigations concerning the phase lag of the flow switching. *J. Wind Engng Ind. Aerodyn.* **43** (1–3), 2047–2056.

SEN, S. & MITTAL, S. 2015 Effect of mass ratio on free vibrations of a square cylinder at low Reynolds numbers. *J. Fluids Struct.* **54**, 661–678.

SEN, S. & MITTAL, S. 2016 Free vibrations of a square cylinder of varying mass ratios. *Procedia Engng* **144**, 34–42.

WILLIAMSON, C. H. K. & GOVARDHAN, R. 2004 Vortex-induced vibrations. *Annu. Rev. Fluid Mech.* **36**, 413–455.

WILLIAMSON, C. H. K. & ROSHKO, A. 1988 Vortex formation in the wake of an oscillating cylinder. *J. Fluids Struct.* **2**, 355–381.

XU, G. & ZHOU, Y. 2004 Strouhal numbers in the wake of two inline cylinders. *Exp. Fluids* **37**, 248–256.

ZDRAVKOVICH, M. M. 1974 Flow-induced vibration of two cylinders in tandem arrangements, and their suppression. In *Proceedings of the International Symposium on Flow Induced Structural Vibrations, Karlsruhe 1972*, pp. 631–639. Springer.

ZDRAVKOVICH, M. M. 1987 The effects of interference between circular cylinders in cross flow. *J. Fluids Struct.* **1**, 239–261.

ZDRAVKOVICH, M. M. 1988 Review of interference-induced oscillations in flow past two parallel circular cylinders in various arrangements. *J. Wind Engng Ind. Aerodyn.* **28** (1–3), 183–199.

ZHAO, M. & YAN, G. 2013 Numerical simulation of vortex-induced vibration of two circular cylinders of different diameters at low Reynolds number. *Phys. Fluids* **25** (8), 083601.

ZHOU, Y. & ALAM, M. M. 2016 Wake of two interacting circular cylinders: a review. *Intl J. Heat Fluid Flow* **62**, 510–537.

ZHOU, Y., FENG, S. X., ALAM, M. M. & BAI, H. L. 2009 Reynolds number effect on the wake of two staggered cylinders. *Phys. Fluids* **21**, 125105.

ZHOU, Y. & YIU, M. W. 2006 Flow structure, momentum and heat transport in a two-tandem-cylinder wake. *J. Fluid Mech.* **548**, 17–48.